ADVANCED FUNCTIONAL MATERIALS
www.afm-journal.de

A Biomimetic, Copolymeric Membrane for Cell-Stretch Experiments with Pulmonary Epithelial Cells at the Air-Liquid Interface

*Ali Doryab, Mehmet Berat Taskin, Philipp Stahlhut, Andreas Schröppel, Darcy E. Wagner, Jürgen Groll, and Otmar Schmid**

Chronic respiratory diseases are among the leading causes of death worldwide, but only symptomatic therapies are available for terminal illness. This in part reflects a lack of biomimetic in vitro models that can imitate the complex environment and physiology of the lung. Here, a copolymeric membrane consisting of poly(ε-)caprolactone and gelatin with tunable properties, resembling the main characteristics of the alveolar basement membrane is introduced. The thin bioinspired membrane (≤5 µm) is stretchable (up to 25% linear strain) with appropriate surface wettability and porosity for culturing lung epithelial cells under air–liquid interface conditions. The unique biphasic concept of this membrane provides optimum characteristics for initial cell growth (phase I) and then switch to biomimetic properties for cyclic cell-stretch experiments (phase II). It is showed that physiologic cyclic mechanical stretch improves formation of F-actin cytoskeleton filaments and tight junctions while non-physiologic over-stretch induces cell apoptosis, activates inflammatory response (IL-8), and impairs epithelial barrier integrity. It is also demonstrated that cyclic physiologic stretch can enhance the cellular uptake of nanoparticles. Since this membrane offers considerable advantages over currently used membranes, it may lead the way to more biomimetic in vitro models of the lung for translation of in vitro response studies into clinical outcome.

1. Introduction

The lung is one of the vital organs in the body that is responsible for gas exchange between air and blood during breathing. Although the prevalence of lung diseases such as chronic obstructive pulmonary disease (COPD) is rising, few causal therapies are available for respiratory diseases due to the complex internal structure and functions of the lung tissue, which cannot easily be recreated in the lab.[1] The availability of preclinical models of lung disease for reliable prediction of clinical outcome is recognized as an important bottleneck for the development of new drugs against lung diseases.[2] Consequently, significant efforts are undertaken to enhance the biomimetic level of currently available in vitro models of lung diseases.[3,4]

The main purpose of the lung is to allow for an efficient supply of oxygen to and removal of carbon dioxide from the red blood cells (erythrocyte). From the trachea, the gas is directed through a complex branching network of conducting

A. Doryab, A. Schröppel, Dr. O. Schmid
Comprehensive Pneumology Center Munich (CPC-M)
Member of the German Center for Lung Research (DZL)
Munich 81377, Germany
E-mail: otmar.schmid@helmholtz-muenchen.de
A. Doryab, A. Schröppel, Dr. O. Schmid
Institute of Lung Biology and Disease (iLBD)
Helmholtz Zentrum München—German Research Center for Environmental Health
Neuherberg 85764, Germany
The ORCID identification number(s) for the author(s) of this article can be found under https://doi.org/10.1002/adfm.202004707.

DOI: 10.1002/adfm.202004707

Dr. M. B. Taskin, P. Stahlhut, Prof. J. Groll
Department of Functional Materials in Medicine and Dentistry and Bavarian Polymer Institute (BPI)
University of Würzburg
Würzburg 97070, Germany
Prof. D. E. Wagner
Department of Experimental Medical Sciences
Lung Bioengineering and Regeneration
Lund University
Lund 22100, Sweden
Prof. D. E. Wagner
Stem Cell Centre
Lund University
Lund 22184, Sweden
Prof. D. E. Wagner
Wallenberg Center for Molecular Medicine
Lund University
Lund 22100, Sweden

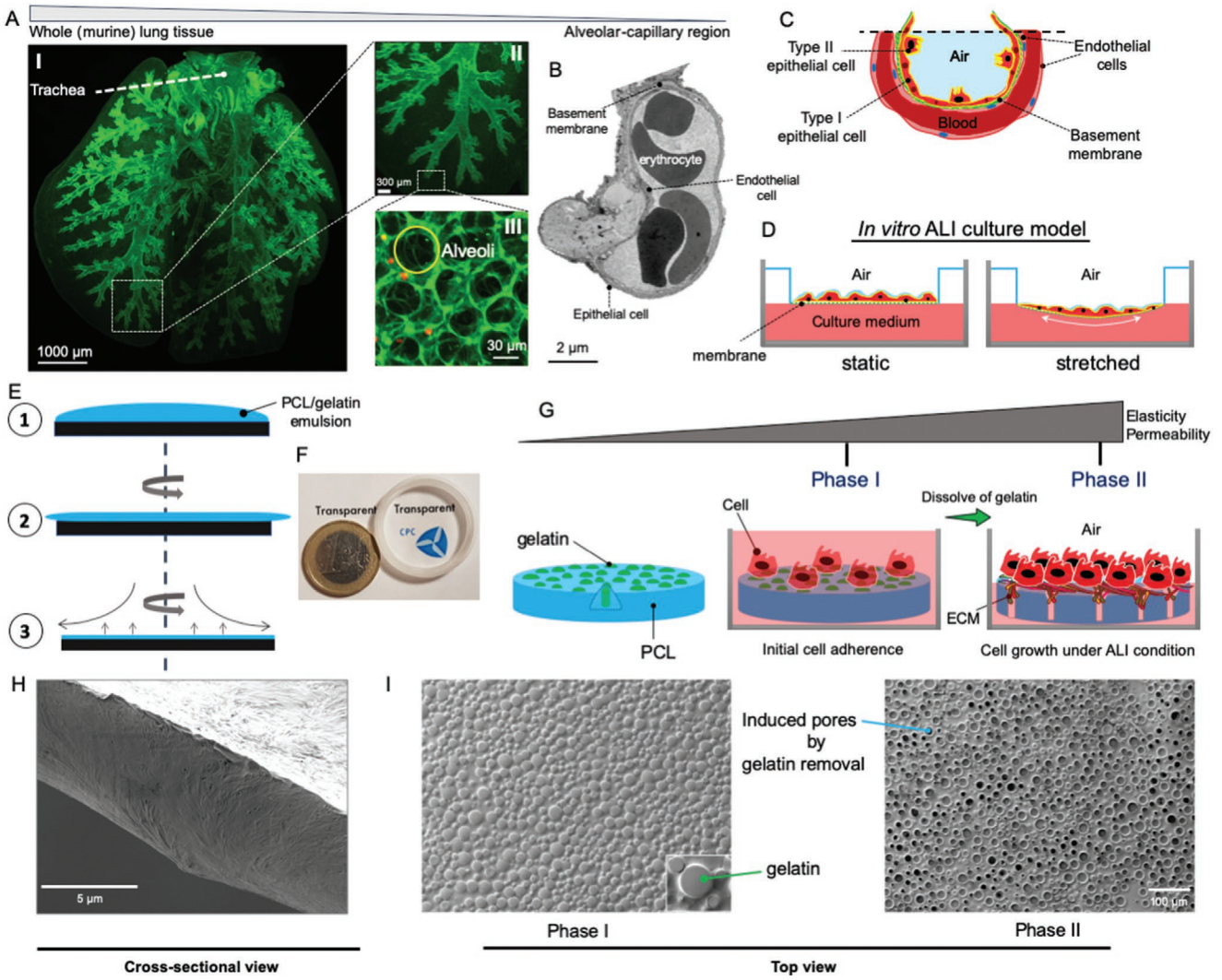

Figure 1. Manufacturing of the BETA membrane. A) A 3D reconstruction of the whole murine lung tissue obtained with light sheet fluorescence microscopy (LSFM) depicting trachea, bronchi, small (terminal) bronchioles (I), distal bronchial tree (II) and 3D honeycomb structure of the alveolar region as observed with confocal microscopy on precision cut lung slices (III). B) Transmission Electron Microscopy (TEM) image of alveolar-capillary region, depicting the alveolar epithelium, capillary endothelium, basement membrane as part of the air–blood barrier, and erythrocyte. Panels of (A,B) reproduced with permission.[6] Copyright 2019, John Wiley and Sons. C) Schematic of lung alveolar region, showing the air-liquid (blood) interface (ALI) in vivo. An ultrathin basement membrane (≤1 µm), which separates epithelial and endothelial cell layers (liquid side). A thin layer of surfactant, which is secreted by type II alveolar epithelial cells, is sitting on the top of epithelial cells to reduce surface tension at ALI in the alveolar region. D) Schematic of in vitro ALI culture models under static and stretch conditions. Cells are seeded on a porous/flexible membrane and air-lifted after forming a confluent cell layer. E) Schematic of the membrane fabrication consisting of poly(ε-)caprolactone (PCL) and gelatin using spin-coating. F) Photograph of the fabricated membrane and a 1-euro coin, showing that it is transparent enough for cell imaging technologies such as live cell imaging and confocal microscopy. G) Depiction of the two phases of the membrane. Phase I: After the spin-coating of a PCL-gelatin mixture, a uniform, non-porous PCL-gelatin membrane is produced, which consists of PCL with embedded "islands" of gelatin serving as adhesion point for cells facilitating subsequent cell proliferation. Spin-coating of a gelatin-PCL mixture results in an initially non-porous PCL-gelatin membrane, where the "islands" of gelatin allow the epithelial cells to grow into a confluent cell monolayer. Phase II: Gradually gelatin is dissolved away by cell culture medium. This opens pores for the nourishment of the cells under ALI conditions, which enhances not only membrane permeability but also elasticity. H) A cross-sectional view of the manufactured membrane. Scale bar is 5 µm. I) SEM image (top view) of the membrane during phase I and phase II. The scale bar is 100 µm.

airways into the alveolar region, where gas exchange takes place (**Figure 1**A). For efficient gas exchange, a micro-scale alveolar-capillary tissue barrier (minimum thickness of ≈1 µm) is required, which essentially consists of an ultrathin basement membrane (≈0.1 µm) covered with a confluent layer of alveolar type-I and type-II (ATI and ATII, respectively) epithelial cells on the apical (air-facing) side and a confluent layer of endothelial cells on the blood side (Figure 1B,C).[5,6] The main functions of this basement membrane include structural support for resident cells as well as transport of nutrients and biomolecules between blood and lung tissue.[6] Thus, the basement membrane of the alveolar region needs to be stiff enough

for supporting the delicate honeycomb structure of the alveolar sacs and yet provide sufficient elasticity to allow for a breathing-induced cyclic stretch at low energy consumption.

Current membrane technologies employed in in vitro lung models focus on structural support for the cells, but are too thick and lack elasticity as compared to basement membranes of the lung.[5,6] Standard cell culture models are grown in multi-well polycarbonate plates under submerged culture conditions, i.e., the cells are completely covered with cell culture media. More advanced, complex, multi-cell, physiologically structured cell cultures of the lung epithelium for studying normal homeostasis and regeneration or co-cultured with disease-specific effector cells (e.g., fibroblasts for pulmonary fibrosis) are commercially available from both healthy donors and patients.[7] These advanced in vitro models are cultured in Transwell inserts under air-liquid interface (ALI) conditions and exposed to aerosolized drugs under dose-controlled conditions.[8–10] On the other hand, these inserts culture the cells on perforated, stiff polyethylene terephthalate (PET) membranes (more rarely polycarbonate or polytetrafluoroethylene (PTFE) membranes are used), which do not mimic the elastic ECM and cyclic stretch conditions in a "breathing" lung, which has been shown to play a key role in the development of chronic lung diseases such as pulmonary fibrosis.[11]

Several cell-stretch devices have been described in the literature, but only a few devices are commercially available and all of them utilize submerged cell cultures.[6] On the other hand, newly designed microfluidic systems for stretch-activated ALI culture conditions have been described 10 years ago but–in spite of significant efforts–are just reaching the marketplace and are not widely used, yet.[12] Most of these cell-stretch devices rely on membranes made out of poly(dimethylsiloxane) (PDMS) since they are considered chemically inert and provide suitable mechano-elastic properties.[12,13] However, they do have disadvantages, which hamper the progress of cell-stretch technologies. PDMS membranes are hydrophobic requiring pre-conditioning of the membrane (e.g., coating with ECM proteins) to enhance wettability and cell adhesion. Achieving a confluent monolayer of epithelial cells on a coated-PDMS membrane is a major challenge since the aggregation and/or dislodgment of cells from the PDMS surface due to protein dissociation often occurs especially for long-term culture conditions and under stretch conditions.[14] Moreover, PDMS adsorbs some drugs and proteins/growth factors contained in the cell culture media and leaching of uncured PDMS oligomers into the culture media can influence cell physiology.[15] Thus, an appropriate membrane providing both optimum cell culture conditions and physicomechanical properties inspired by the microenvironment of alveolar epithelium is still missing, which presents a major obstacle for the development of biomimetic in vitro cell-stretch models of the lung.

Polymeric systems (natural and synthetic-based) are widely used to manufacture suitable scaffolds with biomimetic features for soft tissue applications including lung due to their diversity in chemical groups, allowing for remarkable physical and mechanical properties.[6,16,17]

In this study, we introduce a biphasic copolymeric membrane consisting of gelatin and poly(ε-)caprolactone (PCL) chosen for their cell-conducive and mechano-elastic properties to mimic the microenvironment of alveolar epithelial (AT) cells with respect to important functional features such as mechanical, biophysical, and bioactive properties. This Biphasic Elastic Thin for Air-liquid culture conditions (BETA) membrane facilitates cell adhesion and proliferation without pre-treatment of the membrane and it provides sufficient porosity and biomimetic elasticity as required for in vitro cell-stretch applications under ALI culture conditions. The hybrid membrane is integrated into a stretch-activated lung bioreactor, which allows us to investigate the effect of cyclic mechanical stretch on cell physiology and the transport of nanoparticles across an alveolar barrier model. We also present novel methods for real-time monitoring of cyclic stretch and measuring the elastic modulus of membrane during cell-stretch experiments.

2. Results and Discussion

2.1. The Biphasic Membrane Concept

Mimicking the lung in vitro models of the alveolar barrier often culture a confluent monolayer of epithelial cells under static ALI conditions, where air-exposed epithelial cells are growing on a rigid perforated membrane, which is in contact with cell culture medium on the basal side for the nourishment of the cells (Figure 1D). Only recently, static ALI culture models have been adapted to allow for cyclic stretch conditions, mimicking the mechano-elastic strain exerted during the breathing activity of the lung (Figure 1D).

During the growth of these static or dynamic ALI cell culture models, two main phases can be distinguished; i) an initial phase of cell adhesion, proliferation, and growth of alveolar epithelial cells into a 2D and confluent cell monolayer. Since this is done under submerged cell culture conditions (with cell culture medium in the apical compartment), the membrane does not have to be perforated, yet (phase I). ii) Once a confluent cell layer is formed the cell culture is air-lifted (i.e., cell culture medium is withdrawn from the apical compartment) and left for acclimatization allowing the cells to polarize and secrete protective lining fluid[18] prior to performing the actual cell culture experiments under physiologic ALI conditions (phase II), i.e., a perforated membrane is required for this phase.

Consequently, the "ideal" membrane is tailored toward sequentially meeting the two different sets of specifications corresponding to those two phases of cell culture conditions. For phase I (initial cell growth), the "ideal" membrane is bioactive (i.e., conducive to cell adhesion and growth), wettable and non-porous (prevents cells to migrate into/through the membrane) to facilitate the formation of a planer, confluent epithelial (and endothelial) cell layer under submerged culture conditions. On the other hand, after air-lifting of the cells (phase II), the membrane should be porous/permeable enough to allow for sufficient exchange of nutrients, growth factors, and cell signaling molecules between cells and basal cell culture medium,[19] mimic elasticity/stiffness of the ECM of the lung[20,21] and be resilient to cyclic stretch while being in contact with cell culture medium (Figure 1D). Moreover, the membrane should be as thin as possible (≈0.1 µm in the lung) minimum interference of the membrane with cell

experiments and analytical tools such as microscopy requires the membrane to be as thin as possible (basement membrane of lung: 0.1 µm), optically transparent, chemically inert (no leaching of membrane materials into cell culture medium) and non-adsorptive toward drugs, proteins, and growth factors contained in the cell culture medium. The most widely used current membrane technology tries to accomplish this by using an elastic but hydrophobic material (e.g., PDMS), which requires pre-treatment prior to cell seeding such as chemical and physical modification or coating with ECM proteins (i.e., collagen (or gelatin), fibronectin, and laminin). Moreover, the membrane is always porous as required for phase II, but the pore size is limited to 1–3 µm to prevent epithelial (or endothelial) cells from migrating into or through the membrane during phase I.

Here we pursue a different, biphasic membrane approach, which sequentially adapts the membrane properties to meet the different requirements of the two phases of cell culture conditions during cell-stretch experiments under ALI conditions. We fabricated this biphasic stretchable membrane (BETA) by spin-coating of a copolymer emulsion consisting of PCL and gelatin into a thin (≤5 µm) membrane (Figure 1E–I). Since PCL and gelatin are immiscible in the solvent used here, the spin-coated membrane initially consists of poorly wettable PCL with "islands" of wettable gelatin due to phase separation (Figure 1I). The amide groups of gelatin form hydrogen bonds with water molecules in phase I, improving surface wettability of the initially smooth and nonporous membrane. Moreover, gelatin contains the tripeptide Arg-Gly-Asp (RGD) cell adhesion motif that ligates several integrins and mediates cell attachment.[22] As cells proliferate, they secrete their own ECM allowing them to gradually migrate into the poorly wettable PCL regions and eventually forming a confluent cell layer. Moreover, water-soluble gelatin serves as a sacrificial polymer which is gradually dissolved in cell culture medium, inducing porosity in the originally nonporous membrane as required for phase II (Figures 1I,2A,B and Figure S1, Supporting Information). In addition, selective removal of the relatively stiff gelatin (as compared to the elastic PCL) increases the elasticity of the membrane to a value typically observed for lung tissue (see Section 2.2). Hence, the biphasic membrane concept introduced here leverages the specific properties of a hybrid membrane for the controlled transformation of an initially relatively stiff, nonporous, wettable membrane, which is ideal for the formation of a planar confluent epithelial barrier under submerged culture conditions (phase I), into a porous, elastic and stretchable membrane as required for the cell-stretch experiments under ALI culture conditions (phase II).

2.2. Selection and Characterization of Optimum Membrane

The ideal mixing ratio of the copolymer emulsion (PCL, gelatin) for spin-coating of the membrane was experimentally determined with a design of experiment (DoE) approach using the response surface methodology (RSM) which examines up to 2nd order effects of PCL and gelatin concentration on multiple biophysical and mechanical properties of the membrane. Based on our recently published review paper on physiologic properties of basement membranes of the lung[6] and the membrane requirements listed above, we selected target values of elastic modulus (Young's modulus; 5–10 MPa with ≤10% linear strain), surface wettability (water contact angle WCA ≤70°) and porosity/permeability (sufficient for nutrient exchange; good cell viability in phase II) as well as cytocompatibility (good cell proliferation) as most relevant parameters for optimization of the copolymer mixing ratio.

To this end, we fabricated nine spin-coated PCL/gelatin thin (≤5 µm) membranes in different PCL and gelatin mixing ratios (**Table 1**). All of them formed a uniformly distributed, complex, 3D interconnected gelatin network within a PCL matrix as evidenced by the distribution of gelatin islands (disc-shaped structures) on SEM images of the membrane (Figure 2A and Figure S2A, Supporting Information) and the observed cell viability under ALI conditions. However, PCL/gelatin mixing ratio affects pore size and pore-covered area fraction, which influences cell adhesion, growth, and viability.

The membranes have WCA and porosity in a range of $62.1 \pm 5.2 \leq \text{WCA} \leq 80.6 \pm 2.9$ [°] and $8.80 \pm 1.03 \leq P \leq 28.71 \pm 1.21$ [% of area], respectively (Table 1 and Figure 2C,D). During ≈24 h of contact with cell culture medium, 20–45% of the gelatin is dissolved and the membranes have an elastic (Young's) modulus in a range of $6.25 \pm 0.41 \leq E \leq 14.19 \pm 0.30$ [MPa] depending on PCL/gelatin mixing ratio (Figure 2E) where a membrane with higher PCL concentration is stiffer (lower Young's modulus) and capable to absorb more energy without plastic deformation ($U_r \leq 32$ kPa for ≤7.5% PCL; 65–154 kPa for 10% PCL) (Figure 2F). For the assessment of cytocompatibility, we seeded an alveolar type II-like epithelial cell line (A549) on the membrane. Real-time WST-1 metabolic activity showed that there is no general cytotoxicity for any of the membranes (metabolic activity increases with time; Figure 2G). On the other hand, cells formed a confluent monolayer only on membranes with pores smaller than the size of an individual cell (≈8 µm), i.e., especially for low gelatin concentration (6%), but also for higher gelatin concentration, if the PCL concentration was low (5%) (Figure S3, Supporting Information).

WCA and porosity depend linearly on both PCL and gelatin concentrations (**Figure 3**A,B), while the elastic modulus of the membrane is affected by both one-way mixing ratio and two-way interaction of PCL and gelatin concentrations (Figure 3C). Applying the DoE approach to the experimental data listed in Figure 2 (and Table 1) revealed that the polymer blend consisting of 9.35% PCL and 6.34% gelatin [w/v solvent] provides the optimal membrane properties with respect to co-optimization of elastic modulus, wettability, and porosity (Figure 3D,E).

To validate the fitted model, five membranes with an "optimum" PCL/gelatin mixing ratio (9.35% PCL and 6.34% gelatin) were fabricated and experimentally examined with respect to these parameters. The WCA was found to be 68.8 ± 5.3° which is in-between the limiting values of 119.2 ± 4.2° and 46.8 ± 8.1° measured for PCL and gelatin, respectively (**Figure 4**A). The 2D fractional porosity of the membrane area (in phase II) was determined as 9.4 ± 0.2% with an area-weighted diameter distribution of 4.5 ± 1.7 µm (mean ± SD) (Figure 4B). The elastic modulus of the membrane in phase I and II was 9.01 ± 1.95 and 1.84 ± 0.66 MPa, respectively with an extended reversible

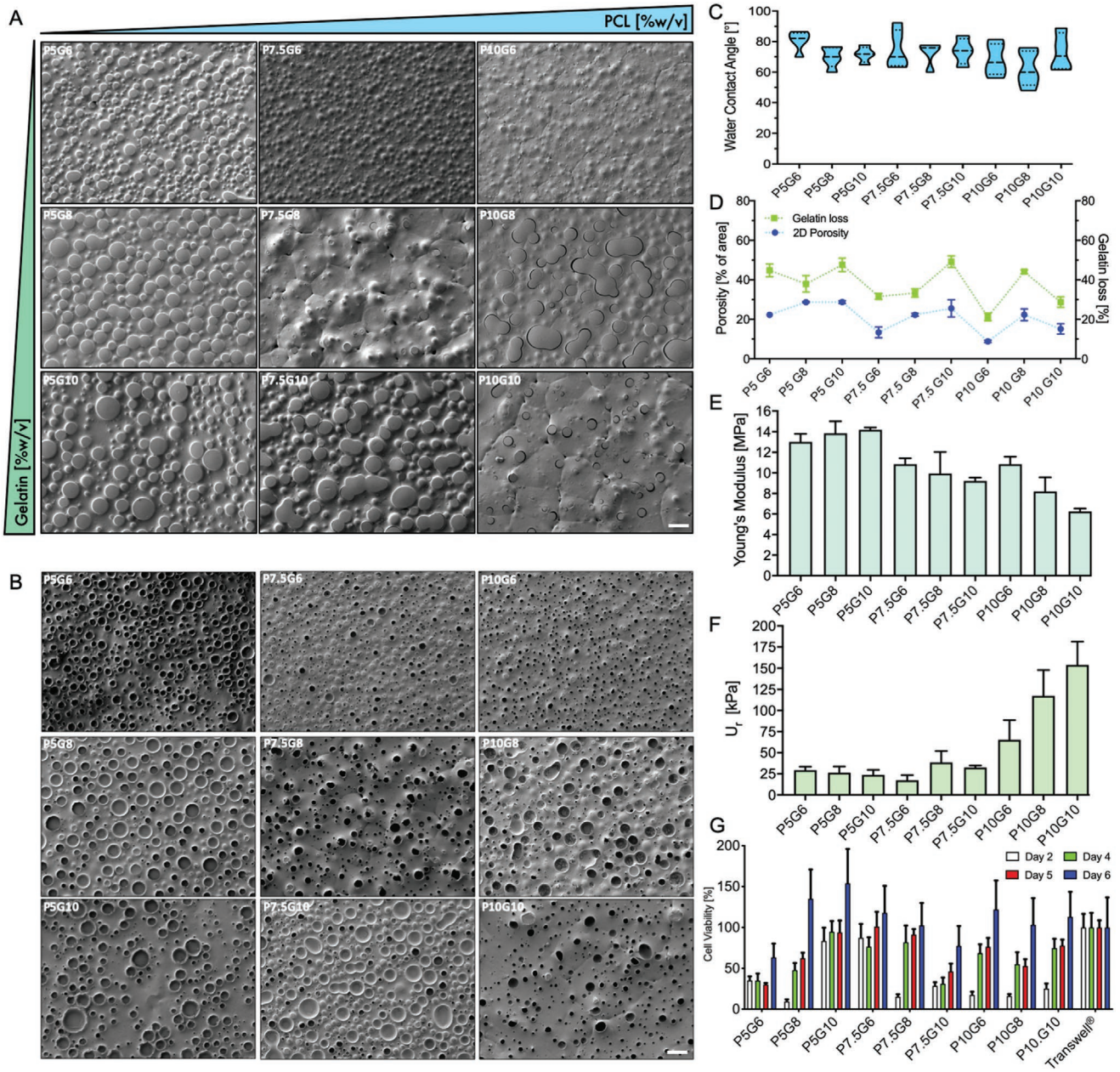

Figure 2. Structural, biophysical and mechanical characterization of the fabricated membranes following a co-optimization strategy. SEM analysis of the fabricated membranes in A) phase I and B) phase II by various combination of PCL (P) and gelatin (G) mixing ratio (Table 1), indicating that higher PCL and lower gelatin concentration result in a narrow-distributed porosity with smaller pore size, which is in favor of ALI culture application. Scale bar is 20 µm. C) Surface wettability of the membrane quantified by WCA. D) Generated porosity after removal of gelatin in phase II quantified by SEM images is a function of the mixing ratio of PCL (p-value ≤0.2) and gelatin (p-value ≤0.03). E) Elastic modulus of the membranes measured by the 1D tensile stress test (phase I). F) The modulus of resilience (U_r) calculated by the area underneath the stress–strain curve up to yield (elastic region). G) WST-1 metabolic activity at days 2, 4, 5, and 6 of cell culturing. Data were baseline-corrected by the OD value of the Corning Costar Transwell cell culture inserts (PET, 12-well, 1.1 cm^2; 0.4 µm pore). Three replicate samples were used for each analysis (n = 3, mean ± SEM).

deformation region up to 25% (linear) (Figure 4C). These results showed no statistically significant differences between model-predicted and experimentally determined parameters (WCA_{exp} vs WCA_{pred}, p-value = 0.834; $Porosity_{exp}$ vs $Porosity_{pred}$, p-value = 0.171; E_{exp} vs E_{pred}, p-value = 0.587).

These five "optimum" membranes (9.35% PCL and 6.34% gelatin) were experimentally examined in more in-depth. A 1D fatigue test was conducted to measure the behavior of the membrane under continued cyclic stretch with an amplitude of 12% linear strain (sinusoidal cyclic stretch) and a frequency of 0.33 Hz (20 cpm). No hysteresis or creep was observed for the maximum test period (4 h), indicating that the BETA membrane can endure cyclic mechanical stretch without any plastic deformation or rupture (Figure 4D). Moreover, 3D Young's modulus of the membrane was measured in the bioreactor during cell culturing after day 1 (1.33 ± 0.14 MPa), day 3 (1.19 ± 0.21 MPa), and

Table 1. Range of PCL/Gelatin mixing ratios and experimental responses entering the design of experiment (DoE) approach to obtain the most biomimetic membrane properties by response surface methodology (RSM) based on Central Composite Design (CCD) arrangement.

Parameters	PCL [%w/v]			GGG Gelatin [%w/v]			WCA [°]	Po Porosity [%]	*E* [MPa]
Levels	–1	0	1	–1	0	1			
[65,66]	5	7.5	10	6	8	10			
Run									
1		5			6		80.6 ± 6.6	22.28 ± 1.82	13.02 ± 1.09
2		10			6		68.0 ± 10.3	8.80 ± 1.03	10.84 ± 1.03
3		5			10		71.5 ± 5.2	28.71 ± 1.21	14.20 ± 0.30
4		10			10		72.9 ± 12.6	15.14 ± 4.53	6.25 ± 0.41
5		5			8		69.9 ± 6.8	28.70 ± 0.53	13.85 ± 1.65
6		10			8		62.1 ± 11.6	22.34 ± 5.12	8.21 ± 1.94
7		7.5			6		74.8 ± 12.5	13.40 ± 4.77	10.85 ± 0.82
8		7.5			10		72.4 ± 8.4	22.29 ± 1.15	9.95 ± 1.94
9		7.5			8		73.8 ± 8.5	25.53 ± 7.57	9.22 ± 0.46

day 6 (0.78 ± 0.24 MPa), revealing that 3D Young's modulus continues to moderately decrease by about a factor of 2 between day 1 and day 6. It is noteworthy that at day 6, 3D Young's modulus (0.78 ± 0.24 MPa) is more than 2-fold lower than the corresponding 1D value (1.84 ± 0.66 MPa), i.e. the BETA membrane is somewhat more elastic under actual cell culture conditions (with cells in place) than determined by standard 1D elastic modulus testing without cells (Figure 4E). The BETA membrane at day 6, which will be used for cell-stretch experiments, remained elastic for 48 h of 3D cyclic stretch (under submerged conditions) with no deformation, rupture, and creep. Thus, this membrane is suitable for cell-stretch experiments for at least up to 48 h, which covers the typically used experimental periods for in vitro cell-stretch experiments.

FTIR analysis of the chemical composition of the BETA membrane in the transition between phase I and phase II showed clear evidence for the removal of gelatin from the membrane (Figure 4F). The characteristic peaks of PCL were approximately observed at 2917 cm^{-1} (asymmetric CH_2), 2850 cm^{-1} (symmetric CH_2), 1722 cm^{-1} (C=O), 1293 cm^{-1} (C–O and C–C), 1239 cm^{-1} (asymmetric C–O–C), and 1162 cm^{-1} (symmetric C–O–C). The FTIR spectrum of the pure gelatin film shows absorption peaks at 3290 cm^{-1} (N–H stretching of amide A), 1629 cm^{-1} (amide I), and 1539 cm^{-1} (amide II).[23,24] All of the characteristic bands of PCL and gelatin were detectable on the membrane before immersion in culture media. Some shifting of bands is observed due to interaction between the ester group of PCL and an amine group of gelatin.[23] After incubation in cell culture medium (phase II), the FT-IR spectrum of porous PCL/gelatin membrane shows only characteristic bands of PCL, indicating that gelatin has been largely washed away (Figure S2B, Supporting Information). The optimum membrane also performed well with respect to cell adherence and growth. A549 epithelial cells formed a confluent monolayer on the membrane (**Figure 5**A,B) with a transepithelial electrical resistance (TEER) of 136 ± 23 Ω cm^2 (under static culture). This relatively low barrier integrity is typical for A549 cells (Figure 4H). Hence, we also tested a bronchial epithelial cell line (16HBE14o–) known to be capable of forming a tighter barrier. Similar to the A549 cells, 16HBE14o– cells also form a uniform confluent monolayer on the membrane (Figure 5C and Figure S4A, Supporting Information), reaching the full barrier integrity as evidenced by the (maximum) TEER value of 452 ± 55 Ω cm^2 after 6 days (Figure 4H), which is in agreement with data reported in the literature.[25] The observed gradual build-up of a confluent 16HBE14o– cell layer is also consistent with the proliferation assay reaching its maximum value on day 7 (Figure 4G). A summary of the characteristics of the optimum membrane is given in Figure 4I. All of these values are in agreement with the target values specified above.

2.3. Improvements over Conventional Membranes

The properties of the (optimum) BETA membrane reported above provide a significant advancement over currently used membranes for ALI cell culture models of the lung, namely PET and PDMS for static and stretch-activated ALI cell culture models, respectively. PET membranes are stiff (Young's modulus of ≈2–3 GPa) but relatively conducive to cell adherence. On the other hand, PDMS is elastic and allows for cyclic cell-stretch, but it is not conducive to cell growth due to its hydrophobic nature (WCA ≥ 105°). The BETA membrane presented here combines conduciveness to cell growth with biomimetic elasticity and resilience to cyclic stretch for at least 48 h (longest time period investigated here). The currently used PET and PDMS membranes are typically at least 10 µm thick and use fixed-sized 1–3 µm pores to provide sufficient permeability for nourishment of cells under ALI culture conditions and to prevent inadvertent migration of epithelial cells from the apical to the basal side (or vice versa for endothelial cells) during phase I.[6] However, 1–3 µm pores are too small to allow for innate cell migration such as infiltration of neutrophils from the blood to the luminal side of the lung epithelium during inflammatory events. The BETA membrane introduced here is not only thinner (<5 µm) but also allows for larger pores during the cell culture experiments (no pores initially; during phase II: 4.5 ± 1.7 µm (mean ± SD) corresponds to a range of 1.1–7.9 µm),

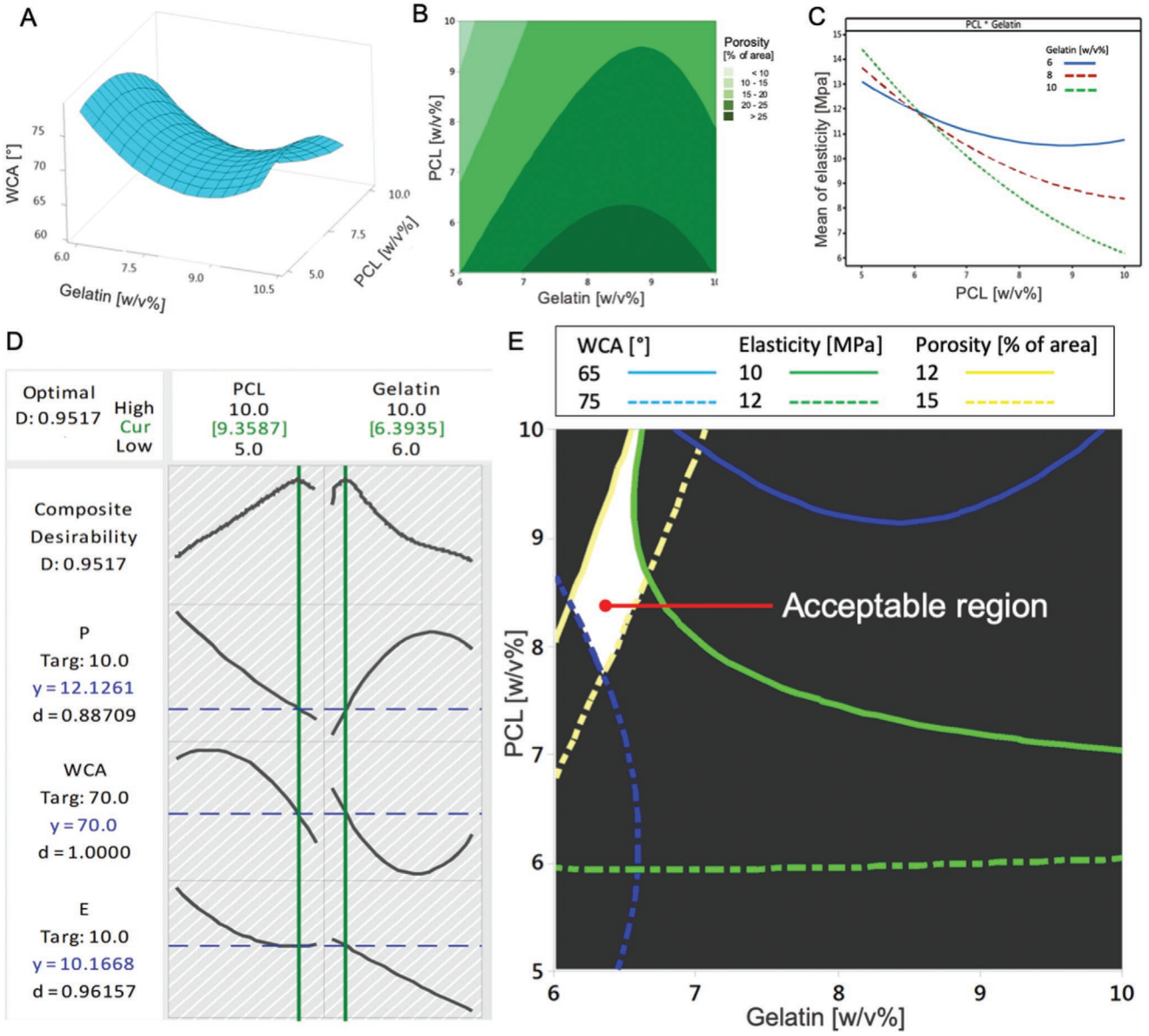

Figure 3. Multi-parameter optimization of PCL-gelatin mixing ratio of the BETA membrane (based on data presented in Figure 2). A) Surface plot of membrane wettability (WCA) for the technically feasible range of PCL and gelatin mixing ratios explored in Figure 2. Both gelatin (p-value ≤0.033) and PCL (p-value ≤0.017) concentrations affect WCA and thus cell attachment. Second-order polynomial regression analysis revealed WCA = 156.6 + 6.7P – 25.5G – 0.6P*P + 1.4G*G + 0.1P*G; R^2 = 0.96. B) Contour plot of porosity (P) versus PCL and gelatin mixing ratio, indicating a linear dependence of porosity on both PCL and gelatin concentration (Porosity = –42.6 – 5.8P + 21.6G + 0.1P*P – 1.3G*G + 0.2P*G; one-way PCL (p-value <0.05) and gelatin (p-value <0.05); R^2 = 0.94)). C) Interaction plot of PCL and gelatin mixing ratio on the elastic modulus (E = 14.5 – 1.3P + 1.5G + 0.2P*P + 0.02G*G – 0.3P*G; R^2 = 0.99), showing that both one-way PCL (p-value ≤0.0001; gelatin p-value ≤0.001) and two-way interaction of PCL and gelatin concentration alter the membrane elasticity. D) The optimization plot, which was provided by the response optimizer demonstrating the composite desirability. E) Weights for WCA, porosity, and elastic modulus were considered as 1, representing equal importance. Overlaid contour plot of membrane response parameters namely elastic modulus (E), water contact angle (WCA), and porosity (P) to select an optimum region of mixing ratios by co-optimization of all relevant variables and responses, reaching the target values (see Section 2.2). The design of experiment (DoE) was applied using Minitab 18 software (Minitab Inc., State College, PA, US). The variables were optimized and the significance of the coefficients was evaluated through the coefficient of determination of the R-squared (R^2) (ability to explain variance) by ANOVA at a 95% confidence level. The experiments were performed with three replicate membranes for each mixing ratio, which were analyzed in a randomized order, to avoid systematic bias.

which reduces inadvertent artifacts of the membrane itself and is likely to allow for trans-membrane migration of migratory cells such as neutrophils (was not investigated here). In addition to these micron-sized pores, the phase II membrane has also numerous much smaller secondary pores (<400 nm) as evidenced by focused ion beam-scanning electron microscopy (FIB-SEM) tomography (Figure 5E). It is also evident from Figure 5E, that the voids left by the sacrificial gelatin provide a connected 3D network of pores suitable for nutrient supply under ALI cell culture conditions. The primary pores are often occupied with cells since this is where the sacrificial gelatin provided the most suitable substrate for cell attachment

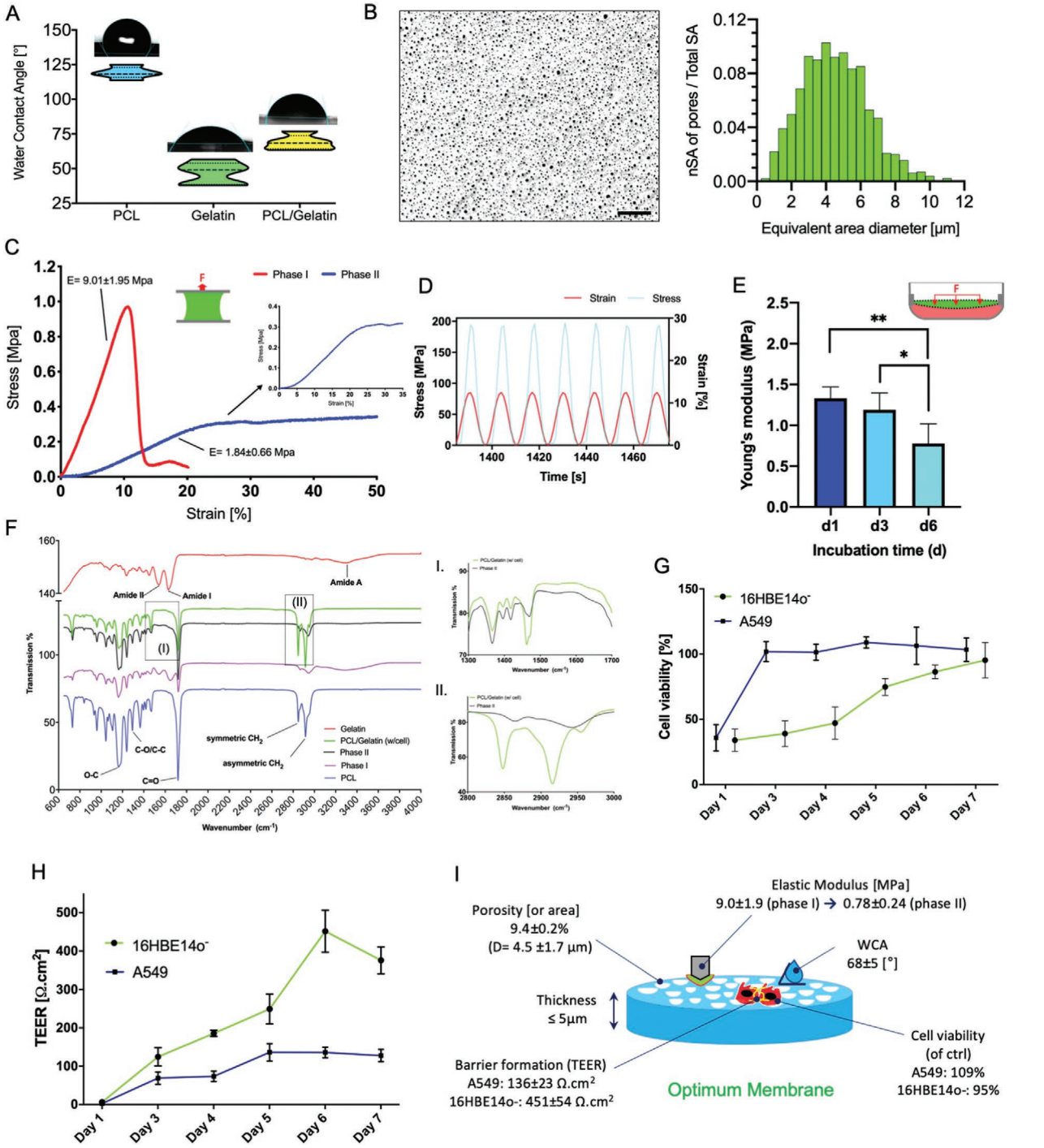

Figure 4. Characterization of the optimized membrane. A) Violin plot of WCA of the membrane compared to the pristine PCL and pristine gelatin films. B) Quantification of porosity of the membrane after day 6 of incubation in cell culture medium (phase II). The pores account for 9.4±0.2% of the membrane surface area and equivalent area diameter of 4.5 ±1.7 µm. Scale bar is 100 µm. C) 1D stress–strain curves of the membrane before (phase I) and after inducing porosity (phase II; 6d in cell culture medium) showing a 4.9-fold increase in elastic modulus after washing out gelatin. D) Segmented fatigue test using sinusoidal cyclic 1D stretch at 12% linear strain at 0.33 Hz for 4 h. E) Time-dependence of 3D Young's modulus of the membrane incubated with cell culture medium in the bioreactor, showing that the elastic modulus of the membrane increases between day 1 and day 6 by ≈30% (phase II). F) FT-IR spectra of pristine gelatin and PCL, PCL/gelatin blend (phase I), porous PCL/gelatin (phase II) and PCL/gelatin membrane after cell culture (6 d incubation). The FT-IR spectrum of the membrane with cells (green curve) and without cells (black curve) in wavenumber of i) 1300–1700 cm^{-1} ii) and 2800–3000 cm^{-1}. G) Time series of cell viability measured by WST-1 assay of A549 and 16HBE14o– cells on the membrane. H) Time series of TEER measurements (barrier tightness) of A549 and 16HBE14o– cells on the membrane. Maximum barrier tightness (confluency) is reached after 6 to 7 days of LLC. K) Schematic of the optimum membrane (9.35% PCL, 6.34% gelatine) showing its unique bio-physicomechanical properties. Data are reported as the mean ± SD. $n \geq 5$; $^{*}P < 0.05$, $^{**}P < 0.001$ by one-way ANOVA with Tukey test.

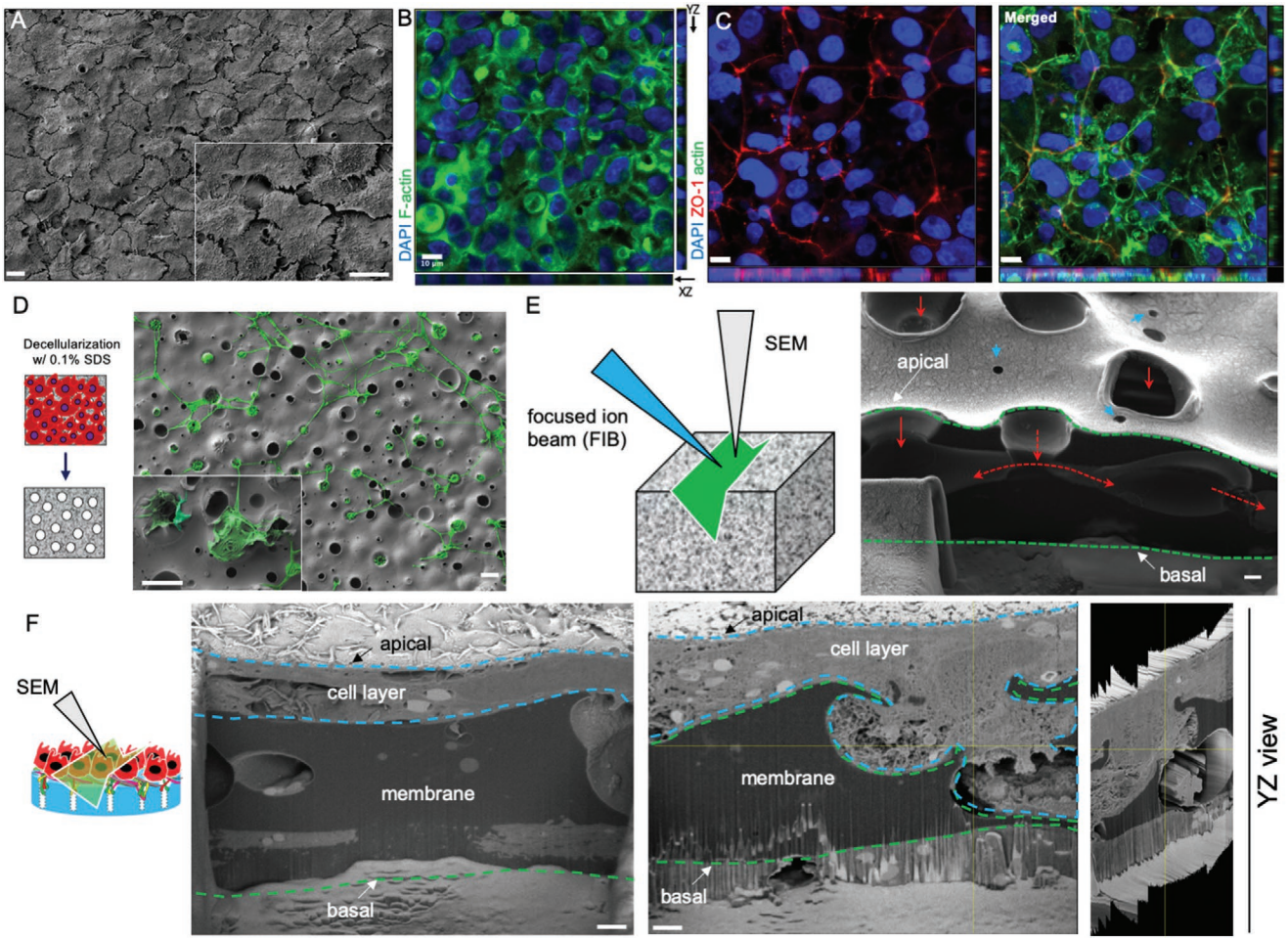

Figure 5. Ultrastructural, morphological and tomographic analysis of cell-membrane interactions. A) SEM image of A549 cells adhering to the surface of the membrane during proliferation on the (optimum) membrane. Scale bar is 10 µm. B) CLSM orthogonal (XY) view and side views of YZ (right) and XZ (bottom), depicting a confluent monolayer of A549 cells (cell seeding density: 1.5×10^5 cells cm^{-2}, 6 days LLC culture) and C) 16HBE14o– cells (cell seeding density: 2×10^5 cells cm^{-2}; incubation: 6 days under LLC and 1 day under ALI conditions) on the membrane. 16HBE14o– cells form tight junctions between cells. Cell nucleus (blue, DAPI), cytoskeleton (green, F-actin), and ZO-1 tight junction (red). Scale bar is 10 µm. D) SEM analysis of the membrane after removal of A549 cells (0.1% SDS) reveals that cells deposit their own ECM (pseudocolored in green) on the BETA membrane. Scale bar is 10 µm. E) Schematic depiction of the focused ion beam (FIB)-SEM tomography for site-specific analysis. FIB-SEM image of the membrane in phase II (without cells). The green dotted lines show the cross-section of the membrane. Red and blue arrows illustrate the primary and secondary pores, respectively. Dashed red arrows show the interconnectivity of the pores in the structure. The scale bar is 1 µm. F) FIB-SEM z-stack image of the cross-section of the membrane populated with A549 cells, showing the cells (blue dotted line) located on the membrane (green dotted line) as a monolayer (left panel) and situated in the micron-sized primary pores (middle and right panel) occasionally even contacting adjacent cells via the 3D pore network. Scale bar is 1 µm.

(Figure 5F). Considering that the innate basement membrane of the alveolar region is ultra-thin (≈0.05 µm), has a substantial fraction of nanopores (<2.5 nm in diameter) and few larger pores (<400 nm), but is fibrous in nature allowing super-micron sized cells to "squeeze" through under certain conditions (e.g., neutrophil influx into the lung during inflammation).[26] The BETA membrane is more biomimetic than conventional engineered membranes, but is still not perfectly representing the basement membrane of the alveolar tissue.

It is also noteworthy that both A549 and 16HBE14o– lung cells secrete their own ECM on the BETA membrane, which contributes to the biomimetic nature of the microenvironment of the cells (Figure 5D) and even more pronounced for 16HBE14o– cells (Figure S4B, Supporting Information). ECM secretion is further evidenced by FT-IR analysis of the decellularized membrane, which reveals new bonds and shifted FT-IR peaks at wavenumbers of 1469, 1461, 2848, 2915, and 2955 cm^{-1} when compared to pristine membranes (Figure 4F-i,ii). Since ECM is a mixture of proteins, lipids, and glycosaminoglycans (GAGs), it is difficult to unambiguously assign a specific functional group to each characteristic peak. However, it has been shown that these peaks can correspond to nucleic acid, ECM proteins, and lipids.[27] We also found some fibrillar structures of ECM on A549 decellularized membranes (Figure 5D). These results, as well as the immunohistochemical identification of ECM proteins such as type I collagen (**Figure 6**B), indicate that epithelial cells do not only proliferate well on the BETA membranes, they also shape their microenvironment by secreting their own ECM components.

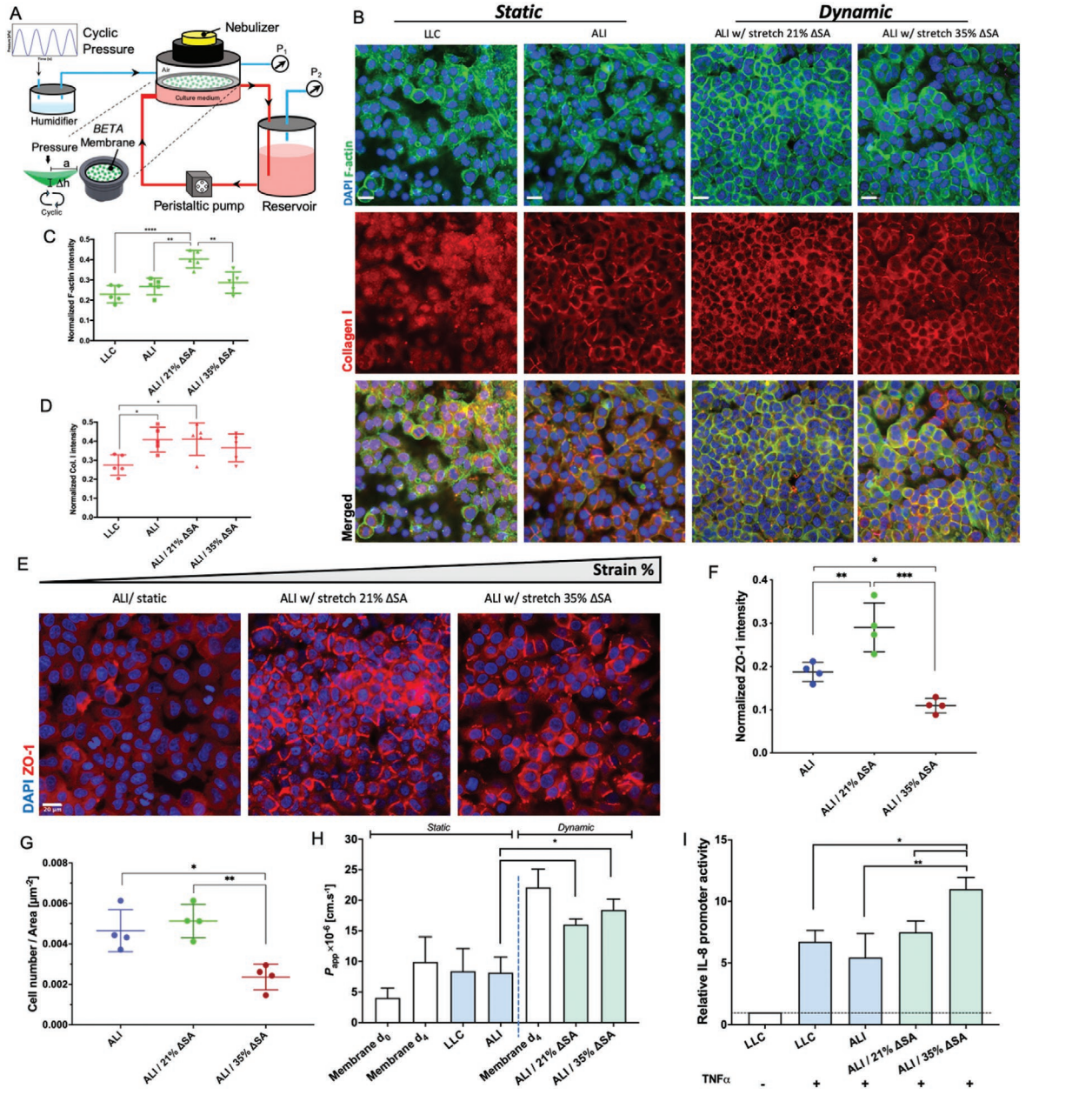

Figure 6. The effect of cyclic mechanical stretch on the cytoskeleton, deposited-ECM, tight junction formation, and barrier integrity. A) Schematic of the in vitro cyclic cell-stretch bioreactor system used in this study. A small positive pressure (maximal 4% above ambient pressure) is applied to the apical side of the membrane, resulting in membrane deformation, which is associated to the volume displacement of cell culture medium into the media reservoir can be monitored via the pressure sensor (P_2) in the medium reservoir. B) Fluorescent CLSM images (obtained for optimum gain/pinhole settings of CLSM) of A549 cells grown on the (optimum) BETA membrane under static (6d LLC and 6d LLC plus 24 h ALI) and dynamic/ALI (21% and 35% ΔSA for 24 h) culture conditions ($n = 5$). Cells under cyclic strain (21% ΔSA) formed more F-actin (green) and collagen I (red). Non-physiologic high levels of strain (35% ΔSA) disrupted the cytoskeleton (no increase in F-actin). On the other hand, deposited collagen I is polymerized under both static and dynamic ALI culture as compared to LLC conditions. Cell nuclei stained with DAPI (blue). Scale bar is 20 µm. These trends are confirmed by quantitative fluorescence analysis (total fluorescence intensity of z-stack–obtained for a given reference gain/pinhole CLSM setting–normalized to the number of cell nuclei) of C) F-actin and D) collagen I in panel B under dynamic ALI and static (LLC and ALI) culture conditions. E) Qualitative (optimum CLSM settings) and F) quantitative CLSM analysis of ZO-1 tight junction formation of A549 cells (reference CLSM settings normalized to the number of cells/nuclei) under physiologic and non-physiologic cyclic mechanical stretch (ALI) conditions ($n = 4$). For each experimental setting, five representative images (z-stacks) were recorded at independent fields of view (region of view: 212.55 µm x 212.55 µm) for each sample. Nuclei (DAPI, blue) and ZO-1 (red). G) The number of cells (nuclei) per area were quantified to investigate the dependence of cell viability under static and stretch conditions. H) Apparent permeability (P_{app}) of a confluent A549 cell monolayer under static (LLC and ALI) and cyclic cell-stretch (21% ΔSA and 35% ΔSA) conditions with respect to FITC-Dextran (4 kDa). Pristine membranes (without cells; white bars) at day 0 and 4 under static and stretch conditions were used as control ($n \geq 4$). I) IL-8 release of pIL8-Luc-A549 cells after stimulating with TNF-alpha (15 ng mL^{-1}). LLC without TNF-alpha stimulation was used as a control ($n \geq 4$). Data are reported as the mean ± SD; $^{*}P < 0.05$, $^{**}P < 0.001$ and $^{****}P < 0.00001$ by one-way ANOVA with Tukey test.

This is important for cell culture studies since it is likely that the secretion of ECM modulates the interaction between the cell cytoskeleton and the membrane/ECM, which are linked by transmembrane receptors so-called integrins that regulate AT cell migration and proliferation.[28] Z-stack FIB-SEM analysis shows the spreading of A549 cells on the membrane, formation of ECM inside pores, and cell-cell interaction via interconnected pores (Figure 5F and Movie S1, Supporting Information). Transmission electron microscopy (TEM) study of the human alveolar wall has shown that alveolar epithelial cells (both type I and II) and human alveolar fibroblasts make contact through gaps in the epithelial basement membrane. In addition, fibroblasts may directly connect the endothelium to the epithelium via apertures in the basement membrane.[29] Mimicry of these aspects may be possible with the BETA membrane presented here.

Furthermore, alveolar epithelial cells such as primary rat alveolar epithelial type II (rATIIs) and human alveolar epithelial type-II like cells (A549) are responsive to membrane stiffness and surface architecture, where softer membranes enhance actin cytoskeletal distribution and diminish tight junction formation[20,21,30] and stiffer membranes increase the formation of F-actin cytoskeleton (Figure S5, Supporting Information), which is consistent with other studies.[31,32] These studies signify the importance of the membrane mimicking the stiffness of the basement membrane of the lung. The membrane under wet conditions has Young's modulus of 0.78 ± 0.24 MPa, which complies with the average of Young's modulus of a single alveolar wall (≈0.30 MPa).[33] As the lungs are under continuous expansion and contraction, and the membrane stretch should remain reversible for at least a few hours, which has been shown to be required for adaptation of cells to cyclic stretch, to the entire lifetime of the cell culture model (here several days). We have shown that the biphasic membrane remains elastic under physiologic cyclic mechanical stretch up to 10% linear strain for 2 days (largest investigated time period).[6]

2.4. Cyclic Mechanical Stretch Regulates Pulmonary Cell Physiology

Cyclic mechanical stretch induces several biological endpoints and activates several pathways involved in the physiology of lung epithelial cells.[6] Here, we implement our (optimum) BETA membrane in the cyclic in vitro cell-stretch (CIVIC) bioreactor, which was designed for culturing of in vitro lung cell models under cyclic mechanical stretch with the possibility of delivering aerosolized substances to the cells, to investigate cellular responses to cyclic stretch under ALI conditions (Figure 6A). It is noteworthy that during physiologic cell stretch experiments cells ALI conditions remain intact remain, i.e., cells do not detach from the membrane and no medium is seeping onto the apical surface. Its unique feature of monitoring the pressure in the apical chamber (P_1) and the pressure in the medium reservoir (P_2) allows for not only for real-time monitoring of amplitude and frequency of cyclic cell stretch during the entire cell-stretch experiment but also of Young's modulus of the membrane. A549 epithelial cells were grown on the membrane to reach confluency and then cyclically stretched (tri-axial (3D), 20 cpm (0.33 Hz)) for 24 h under physiologic (21% ΔSA (surface area); 10% linear) and non-physiologic (35% ΔSA; 16.5% linear) conditions using the CIVIC cell-stretch bioreactor system.

While quantitative confocal laser scanning microscopy (CLSM) analysis showed that the culture condition itself (ALI versus submerged) does not affect F-actin expression, cell-stretch stimulated actin accumulation under physiologic stretch conditions (21% ΔSA strain), but not under overdistension conditions (35% ΔSA strain) (Figure 6B,C). In contrast, secretion of the ECM protein collagen I was stimulated for ALI conditions, but not affected by cyclic mechanical stretch regardless of amplitude (Figure 6B,D). We also found that physiologic stretch induces ZO-1 tight junction formation, while non-physiologic stretch (35% ΔSA) causes a loss of cells (Figure 6G) and a disruption of the integrity of the cell monolayer (Figure 6E,F and Figure S6, Supporting Information). ZO-1 tight junctions were intensified especially at cell–cell junctions, revealing that cyclic physiologic stretch enhances tight junction formation/arrangement (Figure 6E). Moreover, pathologic stretch (35% ΔSA) damaged the cell layer as evidenced by the reduced number of cells possibly due to apoptosis (Figure 6G).

We then studied the paracellular transport of small molecules to evaluate the role of mechanical stretch on barrier integrity. Figure 6H shows the apparent permeability (P_{app}) of FITC-dextran (4 kDa) under stretch conditions compared to static conditions. The permeability of FITC-dextran under submerged (static), ALI (static), ALI 21% ΔSA (dynamic) and ALI 35% ΔSA (dynamic) conditions was measured as $8.48 \pm 3.69 \times 10^{-6}$, $8.18 \pm 2.54 \times 10^{-6}$, $16.03 \pm 0.92 \times 10^{-6}$ and $18.44 \pm 1.74 \times 10^{-6}$ cm s^{-1}, respectively. Apparent permeability analysis indicated that the translocation of (4 kDa) molecules across the cell barrier under ALI conditions is significantly increased under stretch for 24 h compared to static conditions (21% ΔSA vs ALI, $p < 0.03$; 35% ΔSA vs ALI, $p < 0.01$). It is also important to note that the membrane itself has larger permeability under physiologic stretch ($16.01 \pm 0.65 \times 10^{-6}$ cm s^{-1}) than under static conditions ($8.18 \pm 2.54 \times 10^{-6}$ cm s^{-1}), which is likely due to expanding pores (≈1.10-fold larger for 21% ΔSA) and convective dextran transport during the cyclic stretch. Assuming that the transport resistance (≈$1/P_{app}$) of the membrane and the cell barrier are additive, the membrane-corrected permeability of the stretched layer of A549 cells can be determined as 59.5×10^{-6} and 109.9×10^{-6} cm s^{-1} for 21% ΔSA and 35% ΔSA stretch, respectively (Equation (1))

$$P_{app_{cell}} = \left(P_{app\ total} \times P_{app\ membrane}\right) / \left(P_{app\ total} - P_{app\ membrane}\right) \quad (1)$$

This indicates that for non-physiologic stretch (35% ΔSA), the A549 barrier integrity is impaired. It is also instructive to consider P_{app} values (for 4 kDa dextran) for A549 cells cultured on standard Transwell inserts under static conditions. Typical literature values range between 2.5×10^{-6} and 10×10^{-6} cm s^{-1},[34,35] but only very few studies also report P_{app} of the membrane without cells. From Frost et al 2019 (Figure 5 of[34]), one can calculate P_{app} for the membrane (1.70×10^{-5} cm s^{-1} for 12-well Transwell insert; pore size 0.4 μm) and the membrane with cells (7.58×10^{-6} cm s^{-1}) yielding $P_{app} = 1.36 \times 10^{-5}$ cm s^{-1} for A549 cells. This is about 6-fold lower than the value we found for A549

on BETA membrane under physiologic stretch. Thus, cyclic stretch apparently enhances the permeability of A549 cells, but we cannot rule out that the large difference in membrane elastic modulus (≈1000-fold higher as compared to PET) also has an effect on A549 permeability. This effect cannot be assessed from our data since there is no significant difference between P_{app} of the membrane with and without cells (Figure 6H). However, for a PDMS membrane under static conditions in a lung-on-a-chip device, P_{app} of A549 cells was found to be 5.6×10^{-6} cm s^{-1} (as derived from P_{app} of the membrane with (2.5×10^{-6} cm s^{-1}) and without A549 cells (4.5×10^{-6} cm s^{-1}).[34]

We conclude that our results are in general agreement with previously reported results, which validates our BETA membrane for cell-stretch experiments. Formation of actin as one of the main components of the anchored cytoskeleton that is necessary for the maintenance of epithelial barriers can be stimulated by stretch due to an increase in intracellular calcium ion levels that influences epithelial permeability.[36–38] Tight junctions are cell-cell adhesion complexes in epithelial cells that carry out important functions, including controlling paracellular and transcellular transport, maintaining cellular polarity, and regulating a variety of intracellular signals.[39,40] Crucial tight junction proteins in the alveolar epithelium are occludin, ZO-1, and claudin-4.[38] Among them, ZO-1 influences the structure and function of the alveolar epithelial barrier and acts as a connection between transmembrane tight junction proteins and the actin cytoskeleton.[38] It has been shown that a physiological stretch of 8% linear did not affect the integrity of a cell monolayer and ZO-1 formation.[12] On the other hand, a cyclic non-physiologic stretch during mechanical ventilation is playing a pivotal role in disease development (e.g., acute respiratory distress syndrome (ARDS)) via increasing protein permeability, inhibiting tight junction proteins, and disarrangement of actin filaments.[38,41] Cavanaugh et al. showed that the overall expression of ZO-1 is negatively affected by a high level of stretch (37% ΔSA) in rat AT-type II cells.[41] Song et al. also showed that the mechanical overdistension (37% ΔSA strain) causes a disconnection of claudin 4 and 7 from ZO-1 in precision-cut lung slices (PCLS).[42]

Changes in the arrangement of actin cytoskeleton and interaction between F-actin and the tight junction complexes modulate the paracellular permeability.[38–40] Similar to our finding for 4 kDa dextran, it has been reported that cyclic mechanical stretch increases the transport of FITC-sodium (0.4 kDa) in the 16HBE14o– cell line and primary AT cells.[12,43] The apparent permeability for RITC-dextran (70 kDa) is also increased under a physiological stretch of 8% linear strain.[12] High amplitude strain increases the translocation of micromolecules across the alveolar epithelium, which can partly happen through calcium- and actin-dependent mechanisms[37] or by paracellular signaling pathways such as stretch-associated superoxide release.[44]

Albeit stretch-induced enhanced barrier permeability is an important factor for in vitro pharmacokinetic studies, the majority of the research in this field has been carried out under non-physiologic submerged or static ALI conditions.[2,45] There is very little data on the effect of cyclic stretch on the permeability of in vitro barrier models of the lung.

2.5. Inflammatory Response Can Be Activated by Stretch

Interleukin-8 (IL-8) plays a key role in the pathogenesis of inflammatory lung diseases such as ARDS.[46] It has been shown that cyclic stretch promotes IL-8 gene expression and protein release in A549 cells.[47] We used IL-8 release as a marker of deformation-induced inflammatory signaling induced by cyclic stretch. Here, we seeded the IL8-Luc-A549 reporter cell line on the membrane[48] and IL-8 promoter activity was measured using the luciferase assay. IL-8 release of the cells cultured under cyclic stretch of 35% ΔSA for 24 h was significantly higher than under physiologic stretch (21% ΔSA; p-value <0.04), static conditions under both ALI (p-value <0.003) and liquid-liquid culture (LLC) conditions (p-value <0.01), indicating that non-physiologically high stretch (35% ΔSA) activates inflammatory responses (Figure 6I). Again these results agree with previous studies that reported no significant increase in IL-8 secretion by A549 and primary human alveolar epithelial cells under physiologic mechanical strain (10–15% ΔSA strain)[43,49] and intense mechanical stretch (30% ΔSA strain) induced inflammatory mediators such as IL-8 in A549 cells.[47]

2.6. Cellular Uptake of Nano- and Microparticles under Stretch

The effect of cell-stretch on the mechanisms of cellular uptake and paracellular transport of nanoparticles (NPs) is very difficult to study under in vivo conditions. While in vitro studies under static ALI conditions have been performed, to the best of our knowledge, this has not been investigated for cell-stretch conditions, yet. The effect of cyclic stretch on particle uptake was only performed under physiologic conditions (21% ΔSA) since non-physiologically high deformation of the cell layer (35% ΔSA) not only disrupts the tight junctions but also reduces cell viability and loss of cells. While the loss of cells and disruption of tight junctions is expected to substantially enhance transepithelial translocation of particles (Figure 6E,F), reduced cell viability (Figure 6G) inhibits all cellular processes including cellular uptake. Since such a severely injured alveolar cell barrier does not exist in patients, cellular uptake and transepithelial transport of particles were not measured for 35% ΔSA stretch conditions.

Ultrafine ambient NPs (less than 100–300 nm in diameter) are often implicated as particularly hazardous due to their enhanced surface area per mass which has been associated with both acute and chronic lung disease.[50,51] Moreover, NPs smaller than ≈100 nm have a relatively high probability of translocation from the lung to blood circulation (transbarrier transport)[52] which may induce adverse health effects in the secondary target organ (e.g., liver, heart),[53] but it also makes inhaled nanosized particles attractive as drug carriers for both pulmonary and systemic drug delivery.[54]

We chose two sizes (NP: 100 nm diameter; microparticle (MP): 1000 nm) of amine-modified polystyrene (PS-NH_2) particles to investigate the size-dependent effect of physiologic cyclic stretch on cellular uptake dynamics of particles under ALI culture conditions (**Figure 7A**). An aqueous suspension of monodisperse particles (PS-NH_2; 100 and 1000 nm) was

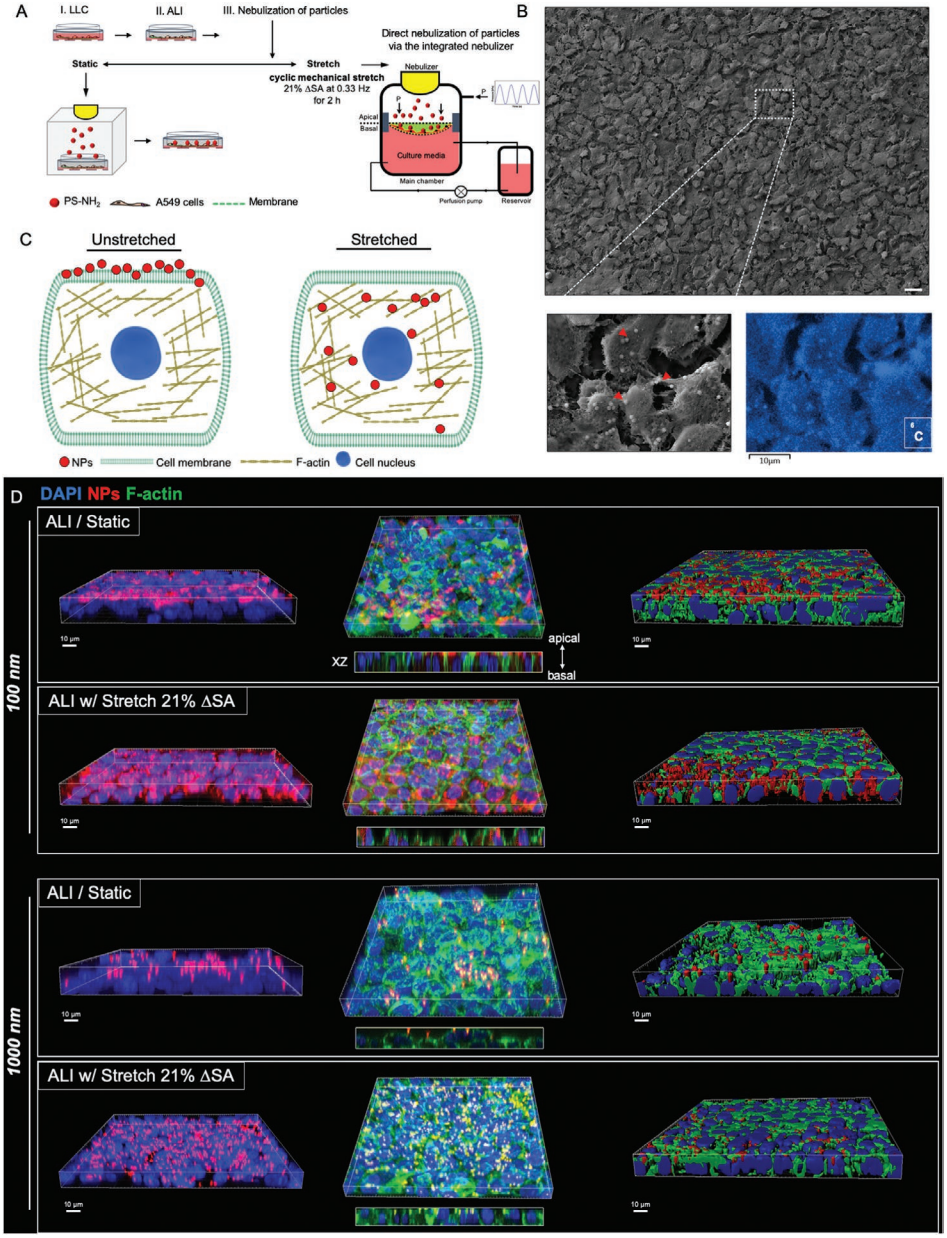

Figure 7. Cell uptake of nano- and microparticles under static and stretch conditions. A) Workflow for particle study. A549 cells (cell density: 2×10^5 cells cm^{-2}) were seeded on the membrane. The cells were cultured under LLC for 4 days and after obtaining a confluent cell monolayer, cells were air-lifted and maintained as ALI culture for 1 day. Amine-modified polystyrene ($PS\text{-}NH_2$) nano- and microparticles (100 and 1000 nm diameter, respectively) are then nebulized onto the cells (within a few minutes) either with the nebulizer of the bioreactor (for cell-stretch conditions) and the VITROCELL CLOUD 6 system (static conditions). After 2 h, the cells were fixed and prepared for CLSM analysis. B) (top) SEM analysis of microparticle (MP) distribution (Red arrow, 1000 nm) on A549 lung cells. Scale bar is 20 µm. (bottom) Detection of MPs (by carbon) using SEM/EDS analysis. Scale bar is 10 µm. C) Schematic depiction of internalization nanoparticles into a cell under static and stretched conditions based on results from panel D. D) 3D reconstruction CLSM images of nano- and microparticles after 2 h under static and physiologic stretch (21% ΔSA) conditions. (left) The perspective (by IMARIS) and XZ (by Fiji) view of CLSM images based on the results of the z-stack and cross-section. (middle) XZ view of CLSM image shows only the NPs (red) and cell nucleus (blue). (right) Surface rendering of CLSM images by IMARIS. These images reveal retention of the MPs near the apical (top) side of the cells for both static and dynamic conditions. Nanoparticles also reside near the apical side of the cell layer under static conditions, but get internalized deeply across the cell membrane and reside in close proximity with actin filaments. Nuclei (DAPI, blue), $PS\text{-}NH_2$ (red), and F-actin (green).

nebulized within a few minutes onto the cells under static/ALI and physiologic cell-stretch/ALI conditions. The exposure process itself does not substantially change the nominal particle diameter. Albeit nebulization increased the nominal particle diameter by about 20% likely due to agglomeration (see Figure S7, Supporting Information), this does not significantly affect our comparison of cellular uptake of nano- versus micron-sized particles. Moreover, the cell-delivered particle

dose of 2.1 μg cm^{-2} was chosen to avoid multi-layered stacking of the particles (agglomeration) by low fractional area coverage of the cells (here: 30% and 3% for 100 and 1000 nm particles, respectively). After 2 h of particle exposure (deposited dose: 2.1 μg cm^{-2}), no cytotoxicity (WST-1 assay) was detected (data not shown) under these conditions. SEM analysis also presented no cell detachment after the nebulization of particles (Figure 7B). Hence, cells were viable enough for reliable cellular uptake measurements.

Localization of particles on the A549 cell layer showed that after 2 h under static conditions, the particles of both sizes (100 and 1000 nm) are located on top of the cell layer often attached to F-actin (Figure 7D and Movies S2–S3, Supporting Information), which is in line with previous studies.[55,56] Under physiological cell-stretch conditions (21% ΔSA strain), the same situation was observed for 1000 nm particles. However, 100 nm NPs were found to efficiently penetrate the cell layer reaching the subcellular compartments in the vicinity of the nucleus and again attaching to the actin filament structure (Figure 7D and Movie S4, Supporting Information).

The knowledge of the effect of stretch on NP internalization in the lung is controversial. In support of our results, Hu et al. showed that physiological mechanical stretch (10% linear strain) enhanced cellular uptake (A549) and internalization of 100 nm PS-NH_2 NPs under ALI conditions.[13] On the other hand, Schmitz et al. reported that physiologic cyclic stretch (15% ΔSA strain) did not increase cellular uptake (A549) of 25 nm SiO_2 NPs under LLC conditions.[49]

For pulmonary epithelial cells, particle uptake primarily occurs via endocytosis, which is limited to particle sizes smaller than ≈500 nm.[57,58] This explains the lack of uptake of 1000 nm particles under both static and cyclic stretch conditions (Figure 7D). Passive para– or transcellular diffusion into and across the cell barrier was ruled out as relevant uptake mechanism by demonstrating that transcellular transport of 100 nm particles was inhibited almost completely at low temperature (4 °C) conditions (data not shown), which implies that an energy-consuming, active cellular mechanism like endocytosis governs cellular uptake. In contrast to previous studies, 100 nm NPs were also found to be attached to the cell surface without penetrating deeper into the cells.[58] Only after cyclic stretch, NPs were abundantly taken up and internalized by A549 cells (Figure 7C). As all previous studies were performed on extremely stiff plastic multi-well plates, this surprising lack of NP uptake under static conditions may be evidence for the impact of membrane elasticity on cellular function and response.

2.7. Advantages of BETA Membrane

Most in vitro cell culture experiments with alveolar epithelial cells cultured under physiologic ALI conditions are performed either on standard PET Transwell inserts (no stretch) or on stretchable PDMS membranes. Alternatively, natural polymers such as collagen and decellularized ECM (derived from pig lung) in combination with synthetic polymers such as poly-L-lactic acid[17] showed an improvement in the physical characteristics of hybrid scaffolds used for lung applications.

Here we presented a biphasic copolymeric membrane concept (PCL/gelatin) which provides optimized conditions for the two different phases of toxicological or pharmacological studies with alveolar barrier models, namely the cell growth (phase I) and cyclic stretch (phase II). The spin-coated PCL/gelatin membrane (9.35% PCL and 6.34% gelatin [w/v solvent]) demonstrated various improved biomimetic features as compared to conventional porous membranes (stiff: PET; elastic: PDMS) such as low interference with transbarrier transport processes, biomimetic elasticity, while maintaining the structural integrity of the membrane even under cyclic stretch, and ease-of-handling.

The bio-inspired membrane manufactured here is ultrathin (thickness ≤ 5 μm), mimicking the total alveolar-capillary barrier thickness (1.1 μm ± 0.1, harmonic mean). The prerequisite for low interference with transbarrier transport processes is i) low membrane thickness (≤5 μm is similar to 1.1 μm of alveolar-capillary tissue (harmonic mean) while PET and PDMS membranes are typically >10 μm), ii) large pore size of up to 8 μm (4.5 ± 1.7 μm (mean± SD) as compared to < 3 μm), and iii) large porosity (9.4 ± 0.2%, instead of 3.5 % or 0.5% for PET membranes with 3 and 0.4 μm pores, respectively (e.g., Corning specification sheet). This results in an apparent permeability (for 4 kDa FITC-dextran) of $8.18 \pm 2.54 \times 10^{-6}$ and $16.03 \pm 0.92 \times 10^{-6}$ cm s^{-1} under static and dynamic (stretch) conditions, respectively, as compared to $4.0 \pm 5.5 \times 10^{-6}$ cm s^{-1} typically reported for PET and PDMS membranes.[34] In addition to the reduced interference of our membrane with transbarrier molecule/particle transport, it is conceivable that up to 8 μm pores (instead of typically 3 μm pores for epithelial cells on PET or PDMS membranes) will facilitate the important features of migration of neutrophils from the basal/blood into the luminal compartment (airside), which is a hallmark of pulmonary inflammation.

Another important aspect of cell functionality is the elastic modulus of the membrane. The BETA membrane has Young's modulus of 0.78 ± 0.24 MPa, which is very similar to alveolar tissue of the lung (0.30 MPa) and much smaller than typical Young's modulus of PDMS membranes (2.61 ± 0.02–3.59±0.11 MPa for 10:1–5:1 base: agent mass ratio).[59] In addition to the high elasticity, the membrane is resilient to fatigue under cyclic stretch for at least up to 48 h, which covers the typically used experimental periods for in vitro cell-stretch experiments and maintains structural integrity not only for small microfluidic lung chips (<mm^2), but also for millifluidic (>cm^2) membranes similar to 6- well, 12-well, and 24-well Transwell inserts. The translucent nature of the manufactured membrane makes it suitable for all optical imaging modalities. Its conduciveness to cell growth does not require physical or chemical functionalization or protein coating of the membrane to stimulate cell adherence and growth.

3. Outlook

The development of even more biomimetic in vitro models of biological organs and barriers is essential for their prediction capacity for human/clinical outcomes with respect to protection and restoration of health. The biphasic copolymer membrane

designed here is capable of closely mimicking several key features of the alveolar-capillary barrier of the human lung.

In this proof-of-concept study with an alveolar type-II like (A549) and bronchial (16HBE14o–) epithelial cell line, we were able to confirm stretch-induced functional changes of these cells reported in the literature. These features include remodeling of the actin cytoskeleton and enhanced barrier function associated with higher levels of tight junction proteins (ZO-1) and permeability (P_{app}) under physiologic stretch conditions (21% ΔSA strain, 0.33 Hz), while non-physiologic stretch (35% ΔSA strain, 0.33 Hz) induced apoptosis, provoked inflammatory responses (IL-8) and disrupted actin cytoskeleton, and barrier integrity. Application of this cell stretch model to aerosolized particles showed that 2 h of physiologic cyclic stretch enhances cellular uptake of NPs (100 nm), but not of MPs (1000 nm). The latter indicates that cyclic stretch does not extend the size limit of 500 nm for endocytic uptake by epithelial cells to 1000 nm.

The BETA membrane introduced here should be tested with advanced cell culture models such as immortalized primary alveolar epithelial cells (hAELVi) and it could be integrated with microfluidic lung-on-a-chip devices to extend their biomimetic features with respect to membrane elasticity, ease of cell growth and reduced membrane thickness. All of these features combined could pave the way for significantly improved in vitro toxicity, drug and pharmacokinetics testing of inhaled substances.

4. Experimental Section

Membrane Fabrication: Poly(ε-caprolactone) (PCL: Sigma-Aldrich, Mn 80 000), and gelatin (Type A from porcine skin, Sigma) were dissolved in TFE ((2,2,2-trifluoroethanol) with ≥99% purity, Roth) and stirred until the emulsion was homogenous. The copolymer emulsion of PCL/gelatin was then added to a homemade spin-coater (2000 rpm) to produce a dense skin layer (Figure 1E–G). The fabricated film was subsequently dried under vacuum (300 mbar) to obtain a uniform layer. The film was then fixed between two polycarbonate holders to create apical and basal chambers. Membranes were sterilized before cell culture experiments with phosphate buffered saline (PBS), ethanol 80% and UV exposure. The film thickness depends on spinning speed, initial viscosity, and evaporation rate.[60] The manufacturing process was optimized to obtain an ultrathin membrane ≤5 µm) (Figure 1H). Design of experiment (DoE) approach using the response surface methodology (RSM)–the central composite design (CCD)–was applied (Minitab 18 software, Minitab Inc., State College, PA, US) to find the optimal mixing ratio of PCL and gelatin (Table 1). The significance and the effect size of variables (concentration of PCL and gelatin) and the corresponding linear and quadratic interactions on the response variables (WCA, porosity, and elastic modulus) were evaluated based on the coefficient of determination (R-squared). Analysis of variance (ANOVA) was used to evaluate whether the model is statistically significant at 95% confidence level.

Membrane Characterization: The morphology of the membranes was observed by scanning electron microscopy (SEM, Zeiss Crossbeam 340, Carl Zeiss AG, Oberkochen, Germany) at an operating voltage of 2 kV. To evaluate cell attachment, the samples were fixed in 6% v/v glutaraldehyde (Sigma-Aldrich) and subsequently post-fixed with 1% OsO4 ((Plano, Wetzlar, Germany)) and 1.5% $K_4Fe(CN)_6$ (Sigma) in 0.1 M CAC buffer for 1 h (4 °C). The samples were then dehydrated in gradient ethanol solutions followed by HDMS (hexamethyldisilazane, Sigma-Aldrich) for 15 min and subsequently mounted onto aluminum stubs, sputter-coated with platinum, and imaged by SEM. ECM materials were pseudocolored in SEM images using the GNU Image Manipulation Program (GIMP 2.10.8) (http://www.gimp.org/).

Focused ion beam (FIB)-SEM tomography (Zeiss Crossbeam 340, Carl Zeiss AG, Oberkochen, Germany) in sectional series (24.5 nm interval) was used to study the internal structures of samples at high resolution (30 kV; 100 and 300 pA). The images were aligned using NIH Fiji (Registration tool) and then reconstructed by IMARIS software (version 9.0; Bitplane, Zurich, Switzerland) and NIH Fiji.

Energy dispersive X-ray spectroscopy (EDS, X-max^N, Oxford instruments) analysis with acceleration voltage of 8 kV was also used to provide qualitative elemental and chemical microanalysis.

To calculate the porosity and the pore diameter size of the membranes, 12 independent fields per sample of SEM images quantified by NIH Fiji macro (Threshold, make binary, watershed and analyze particles).

The water contact angle (WCA) of the membranes was determined with the sessile drop method using an automated contact angle system OCA20 with an image processing system. Deionized water droplets of 1 µL were deposited via a syringe at a velocity of 1 µL s^{-1}. The drop shape was recorded with a high-speed framing camera and measurements were performed 5 s after droplet addition. Five measurements per sample type were performed.

Fourier transform infrared spectroscopy (FT-IR; Nicolet iS 10 FTIR Spectrometer (Thermo Fisher Scientific, Waltham/Massachusetts, USA) was used to analyze the structural properties and chemical changes of the membranes. All spectra were recorded with 32 scans per sample in the attenuated total reflection (ATR) mode in the wavelength range of 400–4000 cm^{-1}.

The mechanical properties of the membranes were characterized using a dynamical mechanical testing instrument (BOSE 5500 system, ElectroForce, Eden Prairie, MN, USA) with a load capacity of 22 N. Film strips membrane (10×10 mm) were stretched at a rate of 0.01 mm s^{-1} until rupture. Sample thickness was measured using the cross-section area of the membranes using SEM. Tensile strength and maximum elongation at the elastic region were calculated. Young's modulus was calculated as the slope of the most linear region of the stress–strain curves in the elastic region. The modulus of resilience (Ur, kPa) which is the area under the strain-stress curve in the elastic region was calculated using the Area Below Curves macro, Sigma Plot 12.0.

Static Cell Culture: Immortalized human alveolar epithelial type-II like A549 cell line was cultured and maintained in Dulbecco's Modified Eagle Medium: Nutrient Mixture F-12 (DMEM/F12, 1:1 v/v, Gibco) supplemented with 10% FCS (Gibco), 1% v/v Pen/Strep (100 U mL^{-1}, Gibco), 1% L-glutamine (2×10^{-3} M, Gibco), and 2-phospho-L-ascorbic acid (0.1×10^{-3} M, Sigma). For cell proliferation study, cell suspension with a cell density of 1×10^5 cells cm^{-2} was seeded on a pre-wetted and sterilized membrane (effective growth area: 1.3 cm^2). Cells first were cultured under liquid–liquid conditions (LLC, 6 days) and then were air-lifted for ALI conditions (24 h).

Bronchial epithelial 16HBE14o– cells were also used for cell model barrier studies such as cell monolayer integrity and TEER measurements. 16HBE14o– cells (cell seeding density: 2×10^5 cells cm^{-2}) were cultured on the membranes (6 days under LLC and 1 day under ALI conditions) in MEM medium (Gibco) supplemented with 10% FCS (Gibco), 1% v/v Pen/Strep (100 U mL^{-1}, Gibco).

Cell viability was measured by WST1-assay. Each membrane was incubated with 1 mL diluted WST1 reagent (Roche, Mannheim, Germany) (1:15) at 37 °C. After 15 min, 150 µL supernatant was transferred to 96-well plate (4 times for each membrane) and was measured in a plate reader (Magellan Tecan) at 450 nm. All the results were normalized to the mean value of blank.

Dynamic Cell Culturing: The CIVIC system was used to apply cyclic stretch to cells grown on the BETA membrane under ALI culture conditions. The CIVIC system is a modified version of the previously described MALI system,[61,62] which has been improved for technical performance mainly related to material stability, membrane fixation, and pressure sealing. While the geometry of the bioreactor system was not changed over the previously described version, some parts were modified to improve the airtightness of the bioreactor chamber and ease of handling. All of the elements, which are in contact with the culture

medium, were manufactured with polycarbonate (PDMS-free materials) to prevent leaching of PDMS to the culture medium. The upgraded polycarbonate holder enables to prevent the membrane sliding and leakage of the culture medium during the cell-stretching experiment. Briefly, the main chamber of the bioreactor consists of an apical (air) and a basal (cell culture media) compartment separated by a membrane for cell growth (Figure 6A). Cell culture medium circulates through the basolateral surface of the membrane using a peristaltic pump to mimic the blood flow (400 µL min^{-1}) while cyclic pressure pulses induced by oscillating airflow in and out of the apical chamber subjects the membrane (and the cells) to a uniform cyclic triaxial strain in surface area (ΔSA). The CIVIC is equipped with a clinically relevant vibrating mesh nebulizer (Aeroneb Pro/Lab, Aerogen Inc, Galway Ireland) for aerosolized substance delivery to the cells. Typically, 10 µL of liquid is nebulized and deposited with a deposition efficiency of 52% onto the ALI cultured cells within ≈1 min. This patented ALICE Cloud technology has become commercially available as VITROCELL Cloud MAX (VITROCELL Systems, Waldkirch, Germany).[61,62]

The elastic modulus of the membrane was measured using the bioreactor system during cell culturing. Two pressure sensors (MPX5050, Freescale Semiconductor, Munich, Germany) were devised in the apical compartment of the bioreactor (P_1) and the headspace of the reservoir chamber (P_2) as depicted in Figure 6A. During cell-stretch, the membrane expands and pushes the culture medium of the basal chamber into the medium reservoir. This compresses the air in the reservoir chamber (ΔV, mL), which can be measured by increased pressure in the reservoir ($\Delta P = P_2 - P_0$), where P_0 is the pressure in both air volumes (ambient air pressure, typically P_0 = 98 kPa) when the membrane is relaxed and V_0 is the corresponding volume of air in the medium reservoir (30 mL). Assuming the membrane motion can be approximated by a spherical cap geometry, the corresponding membrane displacement (ΔV, mL) is associated with the radius (a: 12.6 mm) and axial deflection of the membrane (Δh, cm) (Equations (2) and (3)). The elastic modulus (E, kPa) of the membrane (Young's modulus) can then be calculated from Equation (4).[63]

To study the role of mechanical stretch on cell physiology, A549 cells were seeded on the membrane under dynamic/LLC culture conditions. After 80% of cell confluence, the cells were air-lifted (ALI conditions) and a cyclic mechanical stretch of 21% ΔSA (or 10% radius) and 35% ΔSA (16.5% linear) strain at the 0.33 Hz was subsequently applied to cells to mimic physiologic and non-physiologic conditions, respectively (Equation (5))

$$\Delta V = \Delta P\left(\frac{V_0}{P_0}\right), \text{where } \Delta P = P_2 - P_0 \tag{2}$$

$$\Delta V = \pi \Delta h\left(\frac{a^2}{2} + \frac{\Delta h^2}{6}\right) \tag{3}$$

$$\Delta P' = (P_1 - P_2) = \frac{4E\left(\frac{\Delta h}{a}\right)t}{3a\left(\left(\frac{\Delta h}{a}\right)^2 + 1\right)}\left(1 - \frac{1}{\left(1 + \left(\frac{\Delta h}{a}\right)^2\right)^3}\right) \tag{4}$$

$$\Delta S = S\left(\frac{\Delta h}{a}\right); 0 \le \Delta h \le 0.11\,\text{cm}\,(\,\text{stretch}_{\text{max}}\text{: here 35\% SA}) \tag{5}$$

For physiologic stretch (21% ΔSA); P_1 = 100.5 kPa and P_2 = 99.5 kPa
For non-physiologic stretch (35% ΔSA); P_1 = 102 kPa and P_2 = 100.5 kPa

Immunofluorescence: Cells were fixed in 4% paraformaldehyde (Sigma-Aldrich) for 20 min at room temperature (RT). After washing two times with PBS, cells were permeabilized by 0.3% Triton X-100 (Sigma-Aldrich) in PBS, 10 min at RT. To prevent any unspecific antibody binding, a blocking buffer (5% BSA and 0.1% TritonX-100) was added for 10 min. The cells were then incubated overnight at 4 °C with anti–ZO-1 monoclonal (mouse, 1:100; Invitrogen), anti-collagen type 1 polyclonal (rabbit, 1:100; Rockland) antibodies. After washing with PBS, cells incubated for 1 h in RT with secondary antibody Alexa Fluor 555 goat anti-mouse IgG (1:500; Invitrogen) and Alexa Fluor 488 donkey anti-rabbit IgG (1:500; Invitrogen). The F-actin cytoskeleton and cell nuclei were stained with Phalloidin 594 (1:40) and 4′,6- diamidin-2-phenylindol (DAPI) at 1 µg mL^{-1} in 5% BSA, 0.1% TritonX-100 in PBS, respectively. After rinsing three times with blocking solution, the membranes were embedded in Glycergel (DAKO Schweiz AG, Baar, Switzerland). All cell images were acquired using the confocal laser scanning microscope (LSM710, Carl Zeiss; Oberkochen, Germany), coupled to the Zen2009 software. Images were further processed using the 3D reconstruction IMARIS software (version 9.0; Bitplane, Zurich, Switzerland). For qualitative image analysis (all CLSM figures shown in the manuscript), CLSM images recorded under optimum CLSM settings were presented as selected by the CLSM system (pinhole and gain setting). For quantification, representative 40x images (z-stacks) were recorded under reference gain and pinhole settings of the CLSM (not under sample-specific optimum settings to account for setting-specific CLSM sensitivity) at 5 independent fields of view for each sample (biological replicate). The rectangular tool in Fiji was used to measure the total fluorescence intensity for F-actin, collagen type I, and ZO-1 for each view. Subsequently, the total fluorescence intensity was normalized to the number of cells in each view as determined from the number of nuclei (DAPI staining), which accounts for artefacts due to differences in cell packing.

In Vitro Functional Analysis: Trans-epithelial electrical resistance (TEER) measurements of epithelial cells grown on the optimized membrane were measured periodically using the Millicell-ERS system (Millicell ERS-2, Millipore, USA). The cell-specific resistance can be obtained by subtracting the total resistance across the cell culture membrane with cells from the resistance reading across the acellular membrane. TEER is calculated by multiplying the cell-specific resistance (Ohm, Ω) and the effective surface area of the membrane (cm^2). The experiments were repeated three times and a mean value was determined. For ALI culture, 200 µL of cell culture media was added to the apical part and resistance measured.

To measure the permeability in the apical-to-basolateral direction, first, the culture medium was removed from the basolateral compartment and the cells were washed with PBS. Then, 1 mL of culture media (phenol red-free) and 0.5 mL FITC-Dextran (4 kDa, Sigma-Aldrich) were added to the basolateral and the apical compartment of the epithelial barrier, respectively. Cells were then incubated at 37 °C to equilibrate. Samples from the basolateral were taken at 0, 30, 60, 90, and 120 min (culture media replaced with an equal volume) in a black 96-well plate and were analyzed by the plate reader (Safire 2, Tecan) with excitation and emission wavelengths of 490 and 525 nm, respectively. The apparent permeability coefficient (P_{app}, cm s^{-1}) is calculated using the Equation 6, where dQ/dt is the steady-state flux or the transport rate, A is the surface area of the membrane (cm^2) and C_0 is the initial concentration of FITC-Dextran added to the apical compartment (mg mL^{-1}).[64] Before and after the experiment, TEER was measured to monitor the integrity of the cell monolayer.

$$P_{\text{app}} = \frac{dQ}{dt} * \frac{1}{(A * C_0)} \tag{6}$$

IL-8 Release: The pro-inflammatory IL-8 protein released by the interleukin-8 promoter (pIL8)-reporter A549 cell line was quantified using the luciferase reporter assay ONE-GloTM (Promega, Cat.No. E6120, Mannheim, Germany) according to the manufacturer's instruction. After stimulating cells for 24 h by adding TNF-alpha (15 ng mL^{-1}) to the cell culture medium[8,48] and subsequent stretching (24 h), a mixture of cell lysate and reagent (1:1) measured by the luminometer (96-well format, GLOMAX, Promega, Germany). IL-8 challenge did not impair cell viability (WST-1) or barrier integrity (TEER) (data not shown).

Cell Uptake of Nanoparticle: A549 cells were grown on the BETA membrane (growth area: 4.9 cm^2) until cells reached confluence. Culture media (Phenol red-free DMEM (Gibco) supplemented with 10% FCS (Gibco) and 1% v/v Pen/Strep (100 U mL^{-1}, Gibco)) was aspirated from

the apical part and allowed cells to culture under ALI conditions for 1 day. Afterward, two scenarios were followed I) unstretched and II) stretched conditions (Figure 7A). For static conditions, the membranes were placed in the VITROCELL CLOUD 6 (Vitrocell, Waldkirch, Germany) for nebulization of 100 and 1000 nm amine-modified polystyrene (PS-NH_2) particles (Sigma-Aldrich, St. Louis, USA), diluted by a factor of 10 in 0.3% NaCl. The light intensity-weighted hydrodynamic size distribution (z-diameter) of the PS particles in suspension was measured by dynamic light scattering (DLS) using a Malvern Zetasizer Nano ZS Plus (Model Nr. ZEN3600, Malvern Instruments, UK) both prior and after nebulization (nebulized droplets were collected in a 50 mL Falcon tube). This revealed a ≈20% increase of the (z-average) diameters from 100.4 to 118.8 nm and from 1026 to 1193 nm due to nebulization (see Figure S7, Supporting Information). For the cell-stretch model, particles were nebulized directly onto the cells via the integrated nebulizer in the apical chamber (Figure 7A). The cell-deposited particle dose of 2.1 µg cm^{-2} was determined from the previously determined aerosol deposition efficiency of 52% of the CIVIC system.[61] For this dose, the fractional area coverage was determined to be 30% and 3% for NPs and MPs, respectively (density of PS-NH_2: 1.05 g cm^{-3}). After the nebulization of particles, a cyclic physiologic mechanical stretch (21% ΔSA strain) was applied to the cells. The output rate of the nebulizer and the sedimentation time for both scenarios were 0.5 mL min^{-1} and 3 min, respectively. After 2 h, the cells (under static and stretched conditions) were fixed and prepared for the CLSM analysis.

Statistical Analysis: All data except those designed by Minitab were analyzed using GraphPad Prism 8 (GraphPad Software, La Jolla, CA, USA). Outliers were identified using the Grubbs' method. Student's *t*-test (unpaired, two-tailed) and one-way ANOVA followed by post hoc Tukey's multiple comparison test were used to compare the means of two groups and the means of multiple groups, respectively. Results with a $p < 0.05$ or smaller were considered as a significant level. DoE were designed and the variables were optimized using Minitab 18 software (Minitab Inc., State College, PA, US). ANOVA was applied to evaluate whether the model is statistically significant at a 95% confidence level.

Supporting Information

Supporting Information is available from the Wiley Online Library or from the author.

Acknowledgements

Open access funding enabled and organized by Projekt DEAL.

Conflict of Interest

The authors declare no conflict of interest.

Keywords

alveolar-capillary barrier, cyclic mechanical stretch, hybrid polymers, in vitro cell-stretch model, tunable ultra-thin biphasic membrane

Received: June 2, 2020
Revised: September 10, 2020
Published online:

[1] F. M. E. Franssen, P. Alter, N. Bar, B. J. Benedikter, S. Iurato, D. Maier, M. Maxheim, F. K. Roessler, M. A. Spruit, C. F. Vogelmeier, E. F. M. Wouters, B. Schmeck, *Int. J. Chronic Obstruct. Pulm. Dis.* **2019**, *14*, 1465.
[2] C. Darquenne, J. S. Fleming, I. Katz, A. R. Martin, J. Schroeter, O. S. Usmani, J. Venegas, O. Schmid, *J. Aerosol Med. Pulm. Drug Delivery* **2016**, *29*, 107.
[3] A. Artzy-Schnirman, C. M. Lehr, J. Sznitman, *Expert Opin. Drug Delivery* **2020**, *17*, 621.
[4] S. Ehrmann, O. Schmid, C. Darquenne, B. Rothen-Rutishauser, J. Sznitman, L. Yang, H. Barosova, L. Vecellio, J. Mitchell, N. Heuze-Vourc'h, *Expert Opin. Drug Delivery* **2020**, *17*, 463.
[5] E. R. Weibel, *Respir. Physiol.* **1970**, *11*, 54.
[6] A. Doryab, S. Tas, M. B. Taskin, L. Yang, A. Hilgendorff, J. Groll, D. E. Wagner, O. Schmid, *Adv. Funct. Mater.* **2019**, *29*, 1903114.
[7] A. Doryab, G. Amoabediny, A. Salehi-Najafabadi, *Biotechnol. Adv.* **2016**, *34*, 588.
[8] A.-G. Lenz, T. Stoeger, D. Cei, M. Schmidmeir, N. Semren, G. Burgstaller, B. Lentner, O. Eickelberg, S. Meiners, O. Schmid, *Am. J. Respir. Cell Mol. Biol.* **2014**, *51*, 526.
[9] M. Röhm, S. Carle, F. Maigler, J. Flamm, V. Kramer, C. Mavoungou, O. Schmid, K. Schindowski, *Int. J. Pharm.* **2017**, *532*, 537.
[10] A. Artzy-Schnirman, N. Hobi, N. Schneider-Daum, O. T. Guenat, C.-M. Lehr, J. Sznitman, *Eur. J. Pharm. Biopharm.* **2019**, *144*, 11.
[11] H. Wu, Y. Yu, H. Huang, Y. Hu, S. Fu, Z. Wang, M. Shi, X. Zhao, J. Yuan, J. Li, X. Yang, E. Bin, D. Wei, H. Zhang, J. Zhang, C. Yang, T. Cai, H. Dai, J. Chen, N. Tang, *Cell* **2020**, *180*, 107.
[12] J. D. Stucki, N. Hobi, A. Galimov, A. O. Stucki, N. Schneider-Daum, C.-M. Lehr, H. Huwer, M. Frick, M. Funke-Chambour, T. Geiser, O. T. Guenat, *Sci. Rep.* **2018**, *8*, 14359.
[13] D. Huh, B. D. Matthews, A. Mammoto, M. Montoya-Zavala, H. Y. Hsin, D. E. Ingber, *Science* **2010**, *328*, 1662.
[14] Y. J. Chuah, Y. T. Koh, K. Lim, N. V. Menon, Y. Wu, Y. Kang, *Sci. Rep.* **2016**, *5*, 18162.
[15] K. J. Regehr, M. Domenech, J. T. Koepsel, K. C. Carver, S. J. Ellison-Zelski, W. L. Murphy, L. A. Schuler, E. T. Alarid, D. J. Beebe, *Lab Chip* **2009**, *9*, 2132.
[16] C. P. Laurent, C. Vaquette, X. Liu, J.-F. Schmitt, R. Rahouadj, *J. Biomater. Appl.* **2018**, *32*, 1276.
[17] B. M. Young, K. Shankar, B. P. Allen, R. A. Pouliot, M. B. Schneck, N. S. Mikhaiel, R. L. Heise, *ACS Biomater. Sci. Eng.* **2017**, *3*, 3480.
[18] H.-R. Paur, F. R. Cassee, J. Teeguarden, H. Fissan, S. Diabate, M. Aufderheide, W. G. Kreyling, O. Hänninen, G. Kasper, M. Riediker, B. Rothen-Rutishauser, O. Schmid, *J. Aerosol Sci.* **2011**, *42*, 668.
[19] A. Khademhosseini, R. Langer, *Biomaterials* **2007**, *28*, 5087.
[20] N. Higuita-Castro, M. T. Nelson, V. Shukla, P. A. Agudelo-Garcia, W. Zhang, S. M. Duarte-Sanmiguel, J. A. Englert, J. J. Lannutti, D. J. Hansford, S. N. Ghadiali, *Sci. Rep.* **2017**, *7*, 11623.
[21] M. Koval, C. Ward, M. K. Findley, S. Roser-Page, M. N. Helms, J. Roman, *Am. J. Respir. Cell Mol. Biol.* **2010**, *42*, 172.
[22] N. Davidenko, C. F. Schuster, D. V. Bax, R. W. Farndale, S. Hamaia, S. M. Best, R. E. Cameron, *J. Mater. Sci. Mater. Med.* **2016**, *27*, 148.
[23] S. Gautam, A. K. Dinda, N. C. Mishra, *Mater. Sci. Eng. C* **2013**, *33*, 1228.
[24] S. Yuan, G. Xiong, A. Roguin, C. Choong, *Biointerphases* **2012**, *7*, 30.
[25] K. Luyts, D. Napierska, D. Dinsdale, S. G. Klein, T. Serchi, P. H. M. Hoet, *Toxicol. In Vitro* **2015**, *29*, 234.
[26] C. Hermans, A. Bernard, *Eur. Respir. J.* **1998**, *11*, 801.
[27] M. J. Baker, J. Trevisan, P. Bassan, R. Bhargava, H. J. Butler, K. M. Dorling, P. R. Fielden, S. W. Fogarty, N. J. Fullwood, K. A. Heys, C. Hughes, P. Lasch, P. L. Martin-Hirsch, B. Obinaju, G. D. Sockalingum, J. Sulé-Suso, R. J. Strong, M. J. Walsh, B. R. Wood, P. Gardner, F. L. Martin, *Nat. Protoc.* **2014**, *9*, 1771.
[28] A. Girault, J. Chebli, A. Privé, N. T. N. Trinh, E. Maillé, R. Grygorczyk, E. Brochiero, *Respir. Res.* **2015**, *16*, 100.
[29] F. E. Sirianni, F. S. F. Chu, D. C. Walker, *Am. J. Respir. Crit. Care Med.* **2003**, *168*, 1532.

[30] A. Mammoto, T. Mammoto, M. Kanapathipillai, C. W. Yung, E. Jiang, A. Jiang, K. Lofgren, E. P. S. Gee, D. E. Ingber, *Nat. Commun.* **2013**, *4*, 1759.
[31] B. M. Baker, B. Trappmann, W. Y. Wang, M. S. Sakar, I. L. Kim, V. B. Shenoy, J. A. Burdick, C. S. Chen, *Nat. Mater.* **2015**, *14*, 1262.
[32] A. J. Engler, S. Sen, H. L. Sweeney, D. E. Discher, *Cell* **2006**, *126*, 677.
[33] F. S. A. Cavalcante, S. Ito, K. Brewer, H. Sakai, A. M. Alencar, M. P. Almeida, J. S. Andrade, A. Majumdar, E. P. Ingenito, B. Suki, *J. Appl. Physiol.* **2005**, *98*, 672.
[34] T. S. Frost, L. Jiang, R. M. Lynch, Y. Zohar, *Micromachines* **2019**, *10*, 533.
[35] K. J. Elbert, U. F. Schäfer, H. J. Schäfers, K. J. Kim, V. H. L. Lee, C. M. Lehr, *Pharm. Res.* **1999**, *16*, 601.
[36] H. R. Wirtz, L. G. Dobbs, *Science* **1990**, *250*, 1266.
[37] K. J. Cavanaugh, T. S. Cohen, S. S. Margulies, *Am. J. Physiol.* **2006**, *290*, C1179.
[38] R. Herrero, G. Sanchez, J. A. Lorente, *Ann. Transl. Med.* **2018**, *6*, 32.
[39] E. E. Schneeberger, R. D. Lynch, *Am. J. Physiol.* **2004**, *286*, C1213.
[40] L. González-Mariscal, A. Betanzos, P. Nava, B. E. Jaramillo, *Prog. Biophys. Mol. Biol.* **2003**, *81*, 1.
[41] K. J. Cavanaugh, J. Oswari, S. S. Margulies, *Am. J. Respir. Cell Mol. Biol.* **2001**, *25*, 584.
[42] M. J. Song, N. Davidovich, G. G. Lawrence, S. S. Margulies, *J. Biomech.* **2016**, *49*, 1330.
[43] A. O. Stucki, J. D. Stucki, S. R. R. Hall, M. Felder, Y. Mermoud, R. A. Schmid, T. Geiser, O. T. Guenat, *Lab Chip* **2015**, *15*, 1302.
[44] B. C. DiPaolo, N. Davidovich, M. G. Kazanietz, S. S. Margulies, *Am. J. Physiol.* **2013**, *305*, L141.
[45] O. Schmid, C. Jud, Y. Umehara, D. Mueller, A. Bucholski, F. Gruber, O. Denk, R. Egle, A. Petri-Fink, B. Rothen-Rutishauser, *J. Aerosol Med. Pulm. Drug Delivery* **2017**, *30*, 411.
[46] S. Chollet-Martin, P. Montravers, C. Gibert, C. Elbim, J. M. Desmonts, J. Y. Fagon, M. A. Gougerot-Pocidalo, *Infect. Immun.* **1993**, *61*, 4553.
[47] N. E. Vlahakis, M. A. Schroeder, A. H. Limper, R. D. Hubmayr, *Am. J. Physiol.* **1999**, *277*, L167.
[48] G. J. Oostingh, M. Schmittner, A. K. Ehart, U. Tischler, A. Duschl, *Toxicol. In Vitro* **2008**, *22*, 1301.
[49] C. Schmitz, J. Welck, I. Tavernaro, M. Grinberg, J. Rahnenführer, A. K. Kiemer, C. van Thriel, J. G. Hengstler, A. Kraegeloh, *Nanotoxicology* **2019**, *13*, 1227.
[50] A. Peters, H. E. Wichmann, T. Tuch, J. Heinrich, J. Heyder, *Am. J. Respir. Crit. Care Med.* **1997**, *155*, 1376.
[51] O. Schmid, T. Stoeger, *J. Aerosol Sci.* **2016**, *99*, 133.
[52] W. G. Kreyling, M. Semmler-Behnke, S. Takenaka, W. Möller, *Acc. Chem. Res.* **2013**, *46*, 714.
[53] K. Ganguly, D. Ettehadieh, S. Upadhyay, S. Takenaka, T. Adler, E. Karg, F. Krombach, W. G. Kreyling, H. Schulz, O. Schmid, T. Stoeger, *Part. Fibre Toxicol.* **2017**, *14*, 19.
[54] S. H. van Rijt, D. A. Bölükbas, C. Argyo, K. Wipplinger, M. Naureen, S. Datz, O. Eickelberg, S. Meiners, T. Bein, O. Schmid, T. Stoeger, *Nanoscale* **2016**, *8*, 8058.
[55] S. G. Klein, T. Serchi, L. Hoffmann, B. Blömeke, A. C. Gutleb, *Part. Fibre Toxicol.* **2013**, *10*, 31.
[56] R. Firdessa, T. A. Oelschlaeger, H. Moll, *Eur. J. Cell Biol.* **2014**, *93*, 323.
[57] F. M. Winnik, D. Maysinger, *Acc. Chem. Res.* **2013**, *46*, 672.
[58] I.-L. H. Annika Mareike Gramatke, *J. Nanomed. Nanotechnol.* **2014**, *5*, https://doi.org/10.4172/2157-7439.1000248.
[59] Z. Wang, A. A. Volinsky, N. D. Gallant, *J. Appl. Polym. Sci.* **2014**, *131*, 41050.
[60] D. Meyerhofer, *J. Appl. Phys.* **1978**, *49*, 3993.
[61] D. Cei, A. Doryab, A.-G. Lenz, A. Schröppel, P. Mayer, G. Burgstaller, R. Nossa, A. Ahluwalia, O. Schmid, *Biotechnol. Bioeng.* **2020**, 27600, https://doi.org/10.1002/bit.27600.
[62] D. Cei, Ph.D. Thesis, University of Pisa **2015**.
[63] A. L. Flory, D. A. Brass, K. R. Shull, *J. Polym. Sci., Part B: Polym. Phys.* **2007**, *45*, 3361.
[64] I. Hubatsch, E. G. E. Ragnarsson, P. Artursson, *Nat. Protoc.* **2007**, *2*, 2111.
[65] S. Sharma, S. Mohanty, D. Gupta, M. Jassal, A. K. Agrawal, R. Tandon, *Mol. Vision* **2011**, *17*, 2898.
[66] Y. Zhang, H. Ouyang, C. T. Lim, S. Ramakrishna, Z.-M. Huang, *J. Biomed. Mater. Res.* **2005**, *72B*, 156.